# Low-velocity impact on multi-layered dual-phase steel plates

Jens Kristian Holmen*, Odd Sture Hopperstad, Tore Børvik

*Structural Impact Laboratory (SIMLab), Centre for Research-based Innovation (CRI), Department of Structural Engineering, Norwegian University of Science and Technology, NO-7491 Trondheim, Norway*

## Abstract

In this paper an experimental program investigating the behavior of monolithic and multi-layered configurations of 0.8 mm and 1.8 mm medium-strength steel plates is presented. We have considered impacts by blunt-ended and ogival-ended impactors in the low-velocity regime ($\leq$ 16 m/s). Experimental outputs include measurements of force and velocity, and deformation fields. Force and velocity readings were provided by a strain-gauge instrumented striker, while digital image correlation was used to obtain the displacement field from the rear side of the bottom plate. For the 0.8 mm plates a near linear relationship between the number of layers and the ballistic limit velocity was found. The plates' resistance against perforation was found to be higher for the blunt-ended impactor than for the ogival-ended impactor. This can be explained by the failure mechanisms. The monolithic plates have a higher capacity than layered plates with the same total thickness: this is particularly clear for plates struck by the ogival-ended impactor. The experiments provide ample data to validate the subsequent 3D numerical simulations. The analysis model is double-symmetric in simulations using the ogival-ended impactor, while only a 10° slice of the plate and impactor is needed in simulations using the blunt-ended impactor. A thermoelastic-thermoviscoplastic constitutive relation combined with the Cockcroft-Latham criterion for failure is implemented in IMPETUS Afea Solver, and used in all simulations. The simulations predict the failure modes fairly well, and the numerical results are within the range seen in previous publications. Sensitivity studies regarding friction, mesh refinement, thermal formulation and strain-rate dependence are conducted and discussed.

*Keywords:* Perforation, Experimental validation, 3D-DIC, Finite element analysis, IMPETUS Afea Solver

*Corresponding author. Tel.: +47 73 59 52 02
*Email address:* jens.k.holmen@ntnu.no (Tore Børvik)

## 1. Introduction

Numerous factors influence the penetration and perforation processes in structural impact events, and for each of these factors there are several approaches to investigating the different effects. Impact loading of plates has for a long time been of interest, and the mechanisms of penetration and perforation of different layer configurations due to impact from various projectile shapes are well documented, especially for relatively thick targets, see e.g. Refs [1–4]. More recently, Kpenyigba et al. [5] used thin steel plates, 30 g projectiles and 100 mm spanned plates to perform an experimental, analytical and numerical study on the influence of projectile shape in impact events. It was found that the capacity of plates subjected to impact by hemispherical-ended penetrators is larger than that of plates struck by ogival-ended penetrators and blunt-ended penetrators. A similar numerical study was performed using 52.5 g penetrators by Iqbal et al. [6] where the results indicate a positive correlation between increased target span and ballistic limit. The study indicated that a plate can resist impacts by blunt-ended penetrators better than impacts by ogival-ended penetrators. For the smallest span, however, the opposite was found, showing that a plate's capacity is highly dependent on its configuration. Monolithic targets were found to be stronger than layered targets in contact and layered targets with spacing.

The effect of projectile shape, impact velocity and target configuration on the perforation behavior of thin aluminum plates was studied by Gupta et al. [7]. They found that the plates resisted impacts by hemispherical projectiles better than they resisted impacts from blunt and ogival-shaped projectiles. The double-layered plates performed equally well as the monolithic plates, but a further increase in layers impaired the total capacity. The same authors published another paper where the results from numerical simulations were shown to be sensitive to the mesh refinement [8]. The ballistic properties of blunt and hemispherical projectiles were also studied. Similar to Ref. [7] the plates' capacity against hemispherical projectile impact was found to be the highest.

Work conducted by Woodward and Cimpoeru [9] on the high-velocity perforation processes in monolithic and layered aluminum plates revealed that the ballistic limit of plates struck by conical-shaped projectiles is higher than that of plates struck by flat-ended projectiles. This was found to be independent of the target configuration. The transition from ejection of a target plug for a thick plate to dishing and stretching dominated energy absorption for thinner plates was discussed.

Dey et al. [10] conducted a large experimental and numerical study on the ballistic perforation resistance of monolithic and double-layered Weldox 700E steel plates. Blunt-ended and ogival-ended projectiles

were considered. They found that for blunt-ended projectiles a double-layered configuration of $2 \times 6$ mm performed much better than a monolithic 12 mm configuration. The opposite was found for ogival-ended projectiles, where the monolithic plates performed slightly better than the double-layered configuration. However, the overall protection level increased for layered targets, since the plates' initial perforation capacity using ogival-ended projectiles was considerably higher than the capacity for blunt-ended projectile impact.

Ben-Dor et al. [11] published a review paper in 2012 that gave an overview of some of the most important work regarding layering of target plates in impact engineering. They stated that layering of plates commonly leads to a degradation of ballistic properties and that increasing the velocity reduces the effect of layering. Conclusions from the study highlight the complexity of the problem and that more research is needed to improve our understanding of how target configuration affects the penetration and perforation behavior of protective structures. Further studies concerning low and medium velocity impact are available in the literature (e.g. [12–16]), however, relatively few systematic studies of the effect of projectile shape and layering of thin plates exist. In general, the large number of parameters involved in the penetration and perforation process of layered plates makes it hard to draw definitive conclusions. Varying the span, projectile shape, projectile weight, impact velocity, target material, angle of incidence etc., will inevitably affect the result. It is thus important to establish reliable and validated numerical models in order to study this problem in a systematic way.

In this study, the response of monolithic and multi-layered steel plates subjected to projectile impact in the low-velocity regime is investigated. Configurations consisting of up to four target plates are considered. No adhesives are applied prior to testing, but the plates are in physical contact at the beginning of each test. A dropped-objects-rig is used to strike the targets using blunt-ended and ogival-ended cylindrical impactors. To assess the accuracy of subsequent finite element simulations and to get a better physical understanding of the impact process, digital image correlation (DIC) is used in most of the experiments. Ballistic limit velocities are reported for all configurations.

## 2. Target and impactor materials

Thin plates made of the medium-strength, high-hardening steel Docol 600DL were chosen for this study. The nominal chemical composition of the material can be found in Table 1. The steel has been heat treated to obtain a dual-phase structure of ductile ferrite and strong martensite where the content of

martensite determines the strength of the material. All the plates were produced and delivered by Swedish Steel Ltd. (SSAB). Nominal mechanical properties for the direction transverse to the rolling direction are provided: the yield strength is reported to be between 280 MPa and 360 MPa, while the tensile strength is reported to be between 600 MPa and 700 MPa [17]. Plates of thicknesses 0.8 mm and 1.8 mm are used in the experimental program described in Section 3. In this study, the tensile testing and subsequent material characterization are only performed for the 0.8 mm thick plates.

Tensile tests were conducted at angles 0°, 45° and 90° with respect to the rolling direction of the plate using both an extensometer and DIC functionality [18]. Standard dog-bone specimens with a 70 mm gauge area were used, see Ref. [19] for the geometry. To ensure repeatability, three specimens were tested in each direction. All tests were carried out with a cross-head velocity of 2.0 mm/min which corresponds to an approximate initial strain rate of $5 \times 10^{-4}$ s$^{-1}$. Fig. 1a shows that the material is nearly isotropic with respect to flow stress, but with slight variations in elongation at failure, which is further highlighted in Fig. 2a where the strain at incipient fracture based on DIC measurements is shown as a function of test orientation. As seen, some variation of fracture strain is observed, especially in the 45° direction. Grytten et al. [20] showed that plastic anisotropy is practically insignificant for low-velocity perforation problems. Thus, the limited plastic anisotropy found from the material tests in this study can be ignored and we can safely adopt an isotropic yield function in the material modeling described in Section 5.

The impactors were made of hardened steel with a nominal yield stress $\sigma_0 = 1900$ MPa, fracture strain of about 2.15%, and a Young's modulus $E = 204,000$ MPa [21].

## 3. Experimental work

### *3.1. Test set-up*

Two impactor shapes were considered in this study: a blunt-ended impactor, and an ogival-ended impactor with a caliber radius head (CRH) of 3 - see Ref. [22] for an explanation. Their respective geometries are shown in Fig. 3. They were machined from the same generic projectiles which have been used in several previous research programs on ballistic impact (see e.g. Refs. [21, 23]). All of the experiments reported in this paper were done in an Instron CEAST 9350 dropped-objects-rig with a maximum kinetic energy of 1800 J [24]. We used the standard instrumented striker and striker-holder and these have a combined mass of 5.735 kg. By including the impactors and 4 kg additional weights we achieved a total mass of approximately 10 kg (9.82 kg and 9.78 kg for the blunt-ended and ogival-ended impactors respectively).

For all practical purposes this means that a constant mass was applied regardless of the impactor shape (the difference is only 0.4%). The dropped-objects-rig permits velocities ranging from 0 m/s to 15.5 m/s for masses of approximately 10 kg [24].

Fig. 4 shows how the square target plates of dimensions 400 mm × 400 mm × 0.8 mm were clamped in a circular frame with an inner diameter (span) of 300 mm, ensuring fixed boundary conditions. Clamping was obtained by using 12 equidistant M12 bolts to confine the target plates between two circular frames and to fix this to the dropped-objects-rig. The instrumented striker measured the force at discrete points in time during the experiments. In all tests a load cell with a strain-gauge instrumented tup for interchangeable inserts (in our case blunt-ended and ogival-ended inserts) with a capacity of 90 kN was used. The sensor is placed 150 mm from the tip of the striker. Data was extracted from the sensor every $5 \times 10^{-4}$ ms. Considering that the experiments last between 15 ms and 25 ms we got from 30,000 to 50,000 data points per experiment.

Table 2 provides an overview of the experiments conducted on the different configurations. The main part of the experimental program involved impact testing of the 0.8 mm plates. A total of 33 successful tests were performed on the various plate-impactor configurations with this plate thickness. We considered finding the ballistic limit velocity for all the configurations as the primary task of the experimental program, so a minimum of four individual tests were conducted on each configuration.

A smaller study was done on thicker plates to compare the ballistic limits from the laminated plates to monolithic plates of approximately the same thickness. 1.8 mm thick Docol 600DL plates were delivered by SSAB and we employed the same experimental procedure for these plates as for the 0.8 mm plates. In total, 12 such impact tests were performed. The mechanical behavior of the 1.8 mm thick plates was characterized by Gruben [25] and they were found to be somewhat weaker than the 0.8 mm plates investigated in the rest of this study (the ductility is hardly affected). This is probably due to differences in the cold rolling process and is further commented on in Section 4.

### *3.2. Data processing*

The load cell in the dropped-objects-rig provides enough information to calculate accelerations, and subsequently the velocity and energy for each experiment. The striker velocity just before impact was measured optically by the rig, and this velocity is denoted the initial velocity, $v_i$. Any bias in the force measurements from the load cell was accounted for by subtracting the average of the first 100 data points from each force measurement in the experiment. We find the incremental velocity-change by numerically

integrating the acceleration. Finding the current velocity is done by subtracting the incremental velocity-change from the previous velocity,

$$v_{n+1} = v_n - \left( \frac{F_{n+1} + F_n}{2m_p} - g \right) \Delta t \tag{1}$$

where $v_{n+1}$ is the current velocity, $v_n$ is the previous velocity, $F_{n+1}$ is the current force, $F_n$ is the previous force, $m_p$ is the impacting mass, $g$ is the graviational acceleration, and $\Delta t$ is the sampling time (typically $5 \times 10^{-4}$ ms).

### *3.3. Digital image correlation*

We used the 3D digital image correlation (DIC) software *ECorr* [18] developed at SIMLab to measure the out-of-plane displacement field of the bottom plate as shown in Figs. 5 and 6. From these values we may obtain the strain fields present at the surface of the bottom plate in the experiments [18, 19, 26]. The software uses images from two synchronized cameras, placed as indicated in Fig. 4, to compare the relative displacement of a specimen at deformed stage to an undeformed reference stage. Two Phantom v1610 high-speed cameras with a resolution of $1280 \times 800$ pixels and a frame rate of 16,000 frames per second were used in this study. Before each test the back side of the bottom plate was spray-painted with a black and white speckle pattern. This substantially improved the results from the DIC analyses due to the increased grey-scale contrast.

## 4. Experimental results

### *4.1. Ballistic limit velocities*

From the measured initial and residual velocities of each impact test we can determine the ballistic limit velocities and the ballistic curves for the clamped Docol 600DL steel plates. Impacts with higher initial velocities than the ballistic limit velocity will perforate the target, while impacts with lower initial velocities will be stopped by the plate. Fig. 7a and 7b show the ballistic curves for each layer configuration and impactor shape (tabulated data in Table 3). The data points shown are test results directly plotted into the diagram. The solid lines follow a generalized version of the Recht-Ipson model [27], namely the Lambert equation [1], given as

$$v_r = a \left( v_i^p - v_{bl}^p \right)^{1/p} \tag{2}$$

where $v_{bl}$ is the ballistic limit velocity; $a \leq 1$ and $p$ are empirical constants. The curves in Fig. 7a and 7b are the least-squared-error optimizations of Eq. (2) to the experimental results. All the ballistic limit velocities reported were found by performing this type of optimization. Fig. 8a shows the ballistic limit velocities with respect to impactor shape and total plate thickness. An almost linear increase in the ballistic limit velocity is observed with increasing total plate thickness for both impactor-shapes. It is readily seen that the plates have higher capacity against the blunt-ended impactor than they do against the ogival-ended impactor for the impact conditions investigated in this study, also for the single plate configuration. This is contradictory to what is normally obtained for thicker plates at higher impact velocities, see e.g. Refs. [4, 10]. Figs. 5 and 6 indicate that this is most likely due to substantially larger global bending in the tests with the blunt-ended impactor which is induced by delayed shear localization and subsequent perforation when the initial velocity is as low as it is in this study.

Fig. 8a also shows the ballistic limits from the experiments conducted on the 1.8 mm plates. These values are tabulated in Table 4. In the case of the monolithic plates, multiple experiments were performed with each impactor shape (again see Table 2) so the previously described procedure could be used to determine the ballistic limit. However, the ballistic limit from the double-layered 1.8 mm thick plates were based on a single experiment conducted with each impactor-shape. By solving Eq. (2) with respect to $v_{bl}$ and assuming $a = 1$ and $p = 2$, we found estimates of the ballistic limits for this configuration. These results give a clear indication that the ballistic limit velocity drops for impacts by ogival-ended impactors when the target is layered compared to monolithic targets. This distinct drop was not seen for blunt-ended impactors.

### *4.2. Deformation modes*

Fig. 9 shows timelapses of typical impact tests and Fig. 10 shows pictures of cross sections taken from tests with four layers. In plates struck by the blunt-ended impactor several energy absorbing modes contributed during perforation. First, a transient phase took place before the supports were activated. Second, global bending and membrane stretching were evident from the relatively large deformations out of the plane for all configurations. In this phase the supports were fully activated [28]. Third, plugs were ejected as a result of shearing and local thinning around the circumference of the impactor. In Fig. 5 we see increased maximum deflection due to global bending and increased plastic deformation around the tip of the impactor as the number of plates is increased, and the highest perforation resistance correlates with the largest global deformation.

Comparing the timelapse provided in Fig. 9a to that in Fig. 9b reveals different deformation modes for different impactor shapes. The differences between layered configurations struck with the ogival-ended impactor are not as pronounced as for the blunt-ended impactor. Every plate showed unmistakable petaling which is frequently observed for thin plates impacted by conical-ended or ogival-ended projectiles at low impact velocities [2]. High radial and circumferential tensile stresses are usually responsible for the formation of a star-shaped crack near the tip of the impactor before the thicker part of the impactor creates the distinct petals [3]. In Fig. 10b we see individual petal patterns in each plate and that the petals seem to be slightly skewed relative to the adjacent plate's petals. There are four petals in each plate in every experiment with the 0.8 mm thick plates.

The DIC field maps in Figs. 5 and 6 show out-of-plane deformation of typical configurations just prior to perforation while Fig. 11a shows the out-of-plane deformation of the same configurations as a function of the radial coordinate. These plots clearly display how the deflection increases with total thickness. They also show that the maximum deflection for the blunt-ended impactor is significantly larger than the corresponding maximum deflections for the ogival-ended impactor. The ogival-ended impactor induces limited global deformation (dishing), but distinct petaling as mentioned above. Additional studies regarding petaling can be found in previous work by Wierzbicki [29], and Lee and Wierzbicki [30, 31].

### *4.3. Energy considerations*

We can directly assess the effectiveness of the protective properties of the plates by comparing the energy spent on perforating the given configuration. Fig. 12 shows the absorbed energy (work) per unit thickness for the experiments conducted in this study. These curves are found by assuming that the difference between the kinetic energy prior to perforation ($K_i$) and after perforation ($K_r$) represents the total energy absorption by the plate ($W$). We now get the expression

$$W = \Delta K = K_i - K_r = \frac{1}{2} m_p (v_i^2 - v_r^2) \tag{3}$$

where $m_p$ is the impacting mass, $v_i$ is the initial velocity, and $v_r$ is the residual velocity. Note that we omit the mass of the ejected plug since it in practice is negligible compared to the impacting mass. It has been stated that the energy required to perforate a given configuration is nearly constant for a given projectile, regardless of initial velocity [32]. However, this is not necessarily true for thin plates where the ballistic limit curve does not adhere to the original Recht-Ipson equation (Eq. (2) with $a = 1$ and $p = 2$). The

current series of experiments showed that a near linear relationship between ballistic limit velocity and the number of plates is evident for both impactor-shapes. The same trend is seen for the energy absorption, where the work per unit thickness increases with increasing numbers of layers, especially for the ogival-ended impactor (Fig. 12). This is consistent with the increased global deformation seen in configurations with multiple layers. Iqbal et al. [6] performed a purely numerical study on AA1100-H12 aluminum plates finding that for thin plates ($H/D << 1$) ogival-ended projectile impact is more detrimental to the plate than blunt-ended projectile impact (except for very small target spans). Thus, our experimental results coincide with that study.

### *4.4. Perforation process*

We can analyze the perforation process further by inspecting the force-time plots given in Fig. 13 and Fig. 14. For the tests with the blunt-ended impactor we see in Fig. 13 an initial bending phase, identified as the part of the curve with a steady force increase, before the membrane stretching of the target develops and the force level increases rapidly. This is seen for all plate configurations. When target plate failure occurs we observe an abrupt drop in the force level for each failed plate; this is clearly visible for the single and the double-layered configurations. For the triple-layered and quadruple-layered plates the drop is less clear, but still visible. The force-time curves for the tests with the ogival-ended impactor in Fig. 14 exhibit a steeper climb (relatively) to the maximum force level, and a less dramatic failure process since the initial plate perforation comes almost instantly after impact and petaling is a gradual process. Comparing Fig. 13 and Fig. 14 reveals major differences in the maximum force level and the duration of the respective impacts for the blunt-ended and ogival-ended impactors. The force-time curves from the tests with the blunt-ended impactor rise quickly to a high force, whereas the force-time curves for the ogival-ended impactor in general display lower forces and a delayed time of complete perforation. Note that the maximum force in each configuration is almost constant and rather insensitive to the initial velocity. This is because the maximum force is determined by a mode change from global bending and membrane stretching to localized indentation/perforation of the target.

Fig. 15 displays some typical velocity-time curves where we see that the point of full perforation is more distinct in the tests with the blunt-ended impactor, identified by the acute angle change just when the residual velocity reaches a constant value.

### 4.5. Comparison to thicker plates

In Fig. 8a the ballistic limit velocities determined from experiments on the 1.8 mm thick plates are compared to the ballistic limits of 0.8 mm plates. The results indicate that the capacity of a monolithic plate exceeds the capacity of layered plates of the same thickness for the ogival-ended impactor. In the case of the blunt-ended impactor the effect of layering is negligible. As previously mentioned the 1.8 mm plates are weaker than (but just as ductile as) the 0.8 mm plates due to cold-rolling conditions, meaning that in reality the monolithic plates are even stronger than what appears in Fig. 8a. Comparing these results to the findings by Dey et al. [10] shows that the velocity regime and failure mode seriously affect the perforation resistance of metal plates, and that these need to be carefully considered in each case. Dey et al. studied high-strength steel plates struck by 0.198 kg projectiles (of the same shape as the impactors considered in this study) with ballistic velocities well above 100 m/s. In high-speed impact problems global effects are less pronounced and the failure modes can deviate significantly from what we see in low-velocity impact. This manifests itself in a more localized failure process at high impact velocities.

## 5. Target material characterization

### 5.1. Constitutive modeling

Simulation of impact events such as the ones investigated in this paper requires a material model that accounts for large plastic strains, high strain rates, and temperature softening during plastic flow. Børvik et al. [33] proposed a thermoelastic-thermoviscoplastic constitutive model based on the well-known Johnson-Cook flow stress model. This constitutive relation applied with an extended Voce hardening rule is used in this paper. A brief review of the model is provided in the following.

We assume isotropic material behavior, small elastic strains and no kinematic hardening. However, the plastic strains and rotations can be finite. Thus we can use the $J_2$ flow theory for pressure insensitive materials. We adopt a hypoelastic formulation for the large deformations and decompose the rate-of-deformation tensor $\mathbf{D}$ additively as

$$\mathbf{D} = \mathbf{D}^e + \mathbf{D}^t + \mathbf{D}^p \tag{4}$$

where $\mathbf{D}^e$, $\mathbf{D}^t$ and $\mathbf{D}^p$ are the elastic, thermal and plastic parts, respectively. The elastic and thermal parts are defined by

$$\mathbf{D}^e = \frac{1+\nu}{E}\boldsymbol{\sigma}^{\nabla G} - \frac{\nu}{E}\mathrm{tr}(\boldsymbol{\sigma}^{\nabla G})\mathbf{I}, \tag{5}$$

and

$$\mathbf{D}^t = \alpha \dot{T}\mathbf{I}, \tag{6}$$

where $\nu$ and $E$ are elastic constants, $\boldsymbol{\sigma}^{\nabla G}$ is the Green-Naghdi rate of the Cauchy stress tensor $\boldsymbol{\sigma}$, $\mathbf{I}$ is the second order identity tensor, $\dot{T}$ is the rate of change of the temperature due to adiabatic heating while $\alpha$ is the thermal expansion coefficient of the material.

The yield function is defined in the form

$$f(\boldsymbol{\sigma}, p, T) = \sigma_{eq}(\boldsymbol{\sigma}) - \sigma_y(p, T) \tag{7}$$

where $p$ is the equivalent plastic strain, and $T$ is the temperature. According to the $J_2$ flow theory the equivalent stress is given by

$$\sigma_{eq} = \sqrt{\frac{3}{2}\boldsymbol{\sigma}' : \boldsymbol{\sigma}'}, \tag{8}$$

where $\boldsymbol{\sigma}'$ is the stress deviator calculated as

$$\boldsymbol{\sigma}' = \boldsymbol{\sigma} - \frac{1}{3}\mathrm{tr}(\boldsymbol{\sigma})\mathbf{I}. \tag{9}$$

The yield stress is defined as

$$\sigma_y(p, T) = \left[\sigma_0 + \sum_{i=1}^{2} Q_i(1 - \exp(-C_i p))\right]\left[1 - T^{*m}\right], \tag{10}$$

where the homologous temperature is given as $T^* = (T - T_0)/(T_m - T_0)$, and $m$ is a model parameter controlling the thermal softening. Here $T_m$ is the melting temperature of the material and $T_0$ is the ambient

temperature. $\sigma_0$ is the initial yield stress, and $Q_1$, $C_1$, $Q_2$, and $C_2$ are hardening parameters. By using Eqs. (7) and (8), we can express the plastic rate-of-deformation tensor by means of the associated flow rule as

$$\mathbf{D}^p = \dot{p}\frac{\partial f}{\partial \boldsymbol{\sigma}} = \frac{3}{2}\dot{p}\frac{\boldsymbol{\sigma}'}{\sigma_{eq}}. \tag{11}$$

The equivalent plastic strain rate is defined by

$$\dot{p} = \begin{cases} 0 & \text{for } f \leq 0 \\ \dot{p}_0\left(\left[\dfrac{\sigma_{eq}(\boldsymbol{\sigma})}{\sigma_y(p,T)}\right]^{1/c} - 1\right) & \text{for } f > 0 \end{cases} \tag{12}$$

where $c$ is a material parameter controlling the rate sensitivity, and $\dot{p}_0$ is a user defined strain rate. In the viscoplastic domain, $f > 0$, we obtain an expression for the equivalent stress as

$$\begin{aligned} \sigma_{eq}(\boldsymbol{\sigma}) &\equiv \sqrt{\frac{3}{2}\boldsymbol{\sigma}' : \boldsymbol{\sigma}'} \\ &= \sigma_y(p,T)\left[1 + \frac{\dot{p}}{\dot{p}_0}\right]^c \\ &= \left[\sigma_0 + \sum_{i=1}^{2} Q_i\left(1 - \exp(-C_i p)\right)\right]\left[1 + \frac{\dot{p}}{\dot{p}_0}\right]^c\left[1 - T^{*m}\right]. \end{aligned} \tag{13}$$

The temperature change due to adiabatic heating is calculated using

$$\dot{T} = \frac{\chi}{\rho C_p}\boldsymbol{\sigma} : \mathbf{D}^p = \frac{\chi}{\rho C_p}\sigma_{eq}\dot{p} \tag{14}$$

where $\rho$ is the density, $C_p$ is the specific heat and $\chi$ is the Taylor-Quinney coefficient that represents the proportion of plastic work converted into heat. We typically assume $\chi = 0$ for isothermal conditions and $\chi = 0.9$ for adiabatic conditions (see e.g. [33]).

### *5.2. Failure criterion*

A failure criterion proposed by Cockcroft and Latham (CL) [34] has been applied in this study. The criterion can be easily implemented in finite element codes and it only requires one uniaxial tensile test for

calibration. The criterion as used here is uncoupled from the constitutive model. The CL criterion reads

$$D = \frac{W}{W_{cr}} = \frac{1}{W_{cr}} \int_0^p \langle \sigma_1 \rangle \, \mathrm{d}p, \qquad \langle \sigma_1 \rangle = \max(\sigma_1, 0), \tag{15}$$

where $\sigma_1$ is the major principal stress. Material failure takes place when the damage parameter, $D$, reaches unity. $W_{cr}$ is the failure parameter, which can be found by integrating the major principal stress in a uniaxial tensile test over the entire equivalent plastic strain path to the plastic strain at failure, $p_f$. It can be seen from Eq. (15) that damage will not grow and failure cannot occur if there are no tensile stresses present.

Previously it has been shown that the CL criterion with only one parameter gives equally as good results as more elaborate criteria [35, 36]. Also note that the criterion indirectly accounts for both the deviatoric and hydrostatic stress states, as shown in Fig. 16, through the relation

$$\sigma_1 = \left( \sigma^* + \frac{3 + \mu_\sigma}{3\sqrt{3 + \mu_\sigma^2}} \right) \sigma_{eq}, \tag{16}$$

where $\mu_\sigma$ and $\sigma^*$ are the Lode parameter and the stress triaxiality, respectively, defined in terms of the principal stresses $\sigma_1$, $\sigma_2$, and $\sigma_3$ as

$$\mu_\sigma = \frac{2\sigma_2 - \sigma_1 - \sigma_3}{\sigma_3 - \sigma_1} \tag{17}$$

and

$$\sigma^* = \frac{\sigma_H}{\sigma_{eq}} = \frac{\sigma_1 + \sigma_2 + \sigma_3}{3\sigma_{eq}}. \tag{18}$$

Robustness of the CL criterion with respect to strain rate and temperature has been shown by Børvik et al. [37].

### *5.3. Calibrating the model parameters*

Docol 600DL steel plates have also been used in previous studies. Gruben et al. [19] investigated ductile fracture behavior and Rakvåg et al. [38] considered strain rate effects. The initial yield stress $\sigma_0$ and hardening parameters ($Q_1$, $C_1$, $Q_2$ and $C_2$ in the extended Voce hardening rule) were found to coincide

in these two research programs. The tensile test results presented in Fig. 1a are somewhat inconsistent with the results obtained for the same material (but different batches and thicknesses) in Refs. [19, 38], so a new calibration of the extended Voce hardening rule was made. Data from the extensometer measurements are only valid for displacements up to 4 mm, so by creating a virtual 40 mm extensometer in the DIC software we were able to get force-elongation measurements until specimen fracture. The test that exhibited the median elongation at the point of failure was chosen for further calibration. The scatter in the force level was negligible. A finite element model of the tensile test was made to be run in the explicit version of LS-DYNA 971 [39]. The mesh consists of 1602 8-node trilinear brick elements with selective reduced integration. To reduce the computational time, mass scaling was employed. The model has two elements over the thickness, giving an approximate element size in the gauge area of 0.4 mm.

The optimization itself was conducted in the optimization package LS-OPT [40]. This package reads e.g. LS-DYNA input files and optimizes the parameters of a constitutive relation based on a predefined target curve. The software runs sequential analyses on the same model with varying input parameters with the final goal of minimizing the mean-squared-error between the calculated force-elongation curve and the target curve. In this case we used the parameters $Q_1$, $C_1$, $Q_2$, and $C_2$ of the extended Voce hardening rule which is compatible with the constitutive relation described in Section 5.1. 15 series of 8 simulations, i.e., a total of 120 simulations, were run to obtain the material parameters presented in this study. The initial yield stress at room temperature, $\sigma_0$, was chosen as the stress that gives 0.2% plastic deformation in the reference test. Prior to the optimization an interpolation algorithm was run to ensure equal spacing between the data points of the target curve to prevent weighting of any parts of the curve during the simulations. The target curve (i.e., the force-elongation relation from the 40 mm virtual extensometers) and a simulation run with the optimized input parameters are shown in Fig. 1a. The equivalent stress-equivalent plastic strain curve until necking calculated from the DIC-measurements and the curve resulting from the optimized Voce parameters are shown in Fig. 1b, the agreement is, as seen, good. The hardening parameters that were found using LS-OPT are summarized in Table 5.

The CL failure criterion described in Section 5.2 was calibrated based on the numerical simulations described above. The equivalent plastic strain, $p$, and the major principal stress in the axial direction, $\sigma_1$, were extracted from the element exposed to the largest plastic strain in the finite element analysis of the uniaxial tension test. This element also exhibited the largest value of $W$. The failure strain, $p_f$, was determined from the moment of failure in the numerical model that was adapted to match the force-

elongation curves in Fig. 1a. To find the failure parameter, $W_{cr}$, the major principal stress was integrated over the equivalent plastic strain path. This gave the CL failure parameter $W_{cr} = 473$ MPa (see Table 5). Fig. 2b compares the major surface strain from the representative DIC measurements to a finite element simulation. The correspondence between the two pictures suggests that the strain field and the neck are well captured in the numerical simulation even if the location of necking differs. The spread in elongation and fracture strain shown in Fig. 1a and 2a respectively, suggests a slight spread in $W_{cr}$. Here, $W_{cr}$ has only been calibrated from the tensile test that exhibited the median elongation to failure. This spread will at least to some extent affect the numerical results, but the main trends will remain the same.

The strain rate sensitivity of Docol 600DL was studied by Rakvåg et al. [38]. Because of difficulties involved in testing thin 0.7 mm specimens in a Split Hopkinson Tension Bar (SHTB), they tested 2 mm thick plates. The material was tested at five strain rates in the range 197 $s^{-1}$ to 879 $s^{-1}$. The results revealed pronounced strain-rate sensitivity which increased with plastic strain. Thus the value of the parameter $c$ in the constitutive model (see Eq. (13)) can vary significantly. Rakvåg et al. neglected the rate sensitivity in their main study due to low strain rates. Higher strain rates are expected in this study, so a rate hardening parameter $c = 0.01$ was chosen as a starting point. A study regarding the rate sensitivity is carried out in Section 6.

Table 6 summarizes the physical constants and general model parameters used in the finite element simulations. These are taken from the literature, while $m = 1$ indicates a linear degradation of material strength with increasing temperature which is commonly assumed in impact analyses [37]. The reference strain rate is set to $\dot{p}_0 = 5 \times 10^{-4}\ s^{-1}$ which is close to the initial strain rate in the tensile tests.

## 6. Numerical study

### *6.1. Finite element models*

All simulations were carried out using the explicit finite element code IMPETUS Afea Solver [41]. The program makes use of fully integrated higher order elements including cubic 64-node hexahedrons that are preferential to linear elements when describing bending. Whether we use linear elements, cubic elements, or a combination of the two is a trade-off between computational speed and the desired accuracy. A penalty-based node-to-surface contact algorithm is used in all simulations. Friction is disregarded in most of the simulations, but the effect of the frictional coefficient $\mu$ is investigated by varying its value in a parametric study. The boundaries are fixed by applying translational constraints to all edge nodes in all directions. Full

thermal coupling was employed and a strain rate sensitivity parameter of $c = 0.01$ was chosen based on Ref. [38].

Screenshots of the mesh and impact area of the two models with a single 0.8 mm thick plate are shown in Fig. 17. From the experiments performed in this study we saw that the target plates behaved close to axisymmetric when impacted by blunt-ended impactors. We utilized this by running all analyses with a 10° slice of the entire plate with appropriate boundary conditions applied to the symmetry planes. Most simulations with the blunt-ended impactor were run with 745 cubic hexahedrons in the target plate. In the impact zone we have four elements over the thickness, while we have one element over the thickness in the rest of the plate. Layered plates were modeled with a 0.02 mm gap; this is considered as in contact. Due to the cubic element formulation the number of nodes over the thickness in the impact zone was 13, i.e. a node spacing of 0.067 mm. All simulations with the ogival-ended impactor were run with a double-symmetric model. This was done so that we could describe the observed petaling while keeping the computational time at a reasonable level. Each target plate was discretized into 448 cubic hexahedron elements. The element size was approximately 0.8 mm × 0.8 mm × 0.8 mm in the impact zone and 30 mm × 10 mm × 0.8 mm at the clamped edge. In these simulations the cubic element formulation led to a node spacing in the thickness direction of 0.267 mm. Experience and previous studies have shown that mesh sensitivity is more pronounced in simulations with blunt-ended impactors than in simulations with ogival-ended impactors [16]. Thus, a more refined mesh was chosen for the plates struck by the blunt-ended impactor than for the plates struck by the ogival-ended impactor in this study.

The experiments carried out on the 1.8 mm thick plates were also simulated with the IMPETUS Afea Solver. The general inputs and material constants used for the 1.8 mm plates were identical to the 0.8 mm plates even though the material behavior was slightly different (see Section 3). Twice as many elements over the thickness were used to approximately preserve the node-spacing from the 0.8 mm plates.

Since only the part of the dropped-objects-rig actually striking the target plates was modeled (see Figs. 3 and 17), the added mass from the rest of the rig needed to be accounted for. This was done in the simulations by increasing the density of the impactors, with precautions taken to ensure that the masses matched the real values. The densities $\rho_{\text{blunt}} = 919.35 \times 10^3$ kg/m$^3$ and $\rho_{\text{ogival}} = 1295.23 \times 10^3$ kg/m$^3$ gave the correct respective masses of 9.82 kg and 9.78 kg. The tip of the ogival-ended projectile has been blunted in the numerical simulations (see Fig. 17b). This was done to avoid numerical issues. It is not expected to influence the results.

The hardening and failure parameters for the employed thermoelastic-thermoviscoplastic constitutive model can be found in Table 5, whereas the physical constants and model parameters are given in Table 6. The implementation of the CL criterion in IMPETUS Afea Solver states that when the damage parameter, $D$ in Eq. (15), has evolved from 0 to 1 in an integration point, the integration point loses its shear strength and we have local material failure. After local failure in a number of integration points (16 for cubic hexahedrons) the element is removed from the analysis. This is defined as element erosion.

The simulation times were highly dependent on the termination time of the analysis at hand, which is difficult to determine a priori. In many cases the analyses have been run longer than necessary. If we disregard this, most of the simulations took around 10 hours to run on a NVIDIA Tesla Kepler K20c GPU.

### *6.2. Finite element results*

Fig. 7 compares the ballistic limit curves from the numerical simulations to the experiments. Analyses have been run with identical initial velocities as in the experiments. Hence, each experiment has a corresponding simulation. Some additional simulations were run where this was deemed necessary to determine the entire ballistic curve. Plots from two typical simulations are shown in Figs. 18 and 19. The former illustrates how global deformation precedes membrane stretching and plug ejection in the plates struck by the blunt-ended impactor, while the latter shows the formation of petals which were also observed in the experiments on plates struck by the ogival-ended impactor.

Comparing Fig. 8a to Fig. 8b shows that the simulations reflect the trends observed in the experiments. However, the range in the ballistic limits is smaller in the numerical simulations than in the experimental data. This is due to an underestimation of the ballistic limit velocities for the multi-layered plates struck by the blunt-ended impactor in the numerical simulations. In addition, Fig. 8b shows the numerical results for the 1.8 mm plates. Also these results are in general underestimated and for the double-layered plates the ballistic limit velocity is actually higher for plates struck by the ogival-ended impactor than for the blunt-ended impactor.

Table 3 compares the ballistic limit velocities from the simulations to the experiments. The underestimation of the ballistic limit velocities for the blunt-ended impactor is seen, especially for the quadruple-layered plates. This means that the results are on the conservative side, which is preferred in design situations. The simulations involving the ogival-ended impactor gave excellent results in terms of ballistic limit velocity for the double-layered and triple-layered plates, but an underestimation of the capacity for the quadruple-layered plates and an overestimation of the capacity for the single plates. Table 4 compares the simulations

to the experiments for the 1.8 mm plates. The trends are the same as for the 0.8 mm plates with the same discrepancy in ballistic limit velocity for the different impactor shapes.

Fig. 20a compares the force-time curve from a simulation to a typical experiment with the blunt-ended impactor, $v_i = 5.9$ m/s in both cases. The initial increase in force level, where bending dominates the behavior, is very similar in the simulation and the experiment. However, after about 1.5 ms the force level develops faster, and to a higher maximum level, in the simulation. Failure occurs prematurely, leading to higher predicted residual velocities than those found in the corresponding experiments.

Comparing the simulation in Fig. 20b to the corresponding experiment with the ogival-ended impactor ($v_i = 3.6$ m/s) reveals that the initial increase in the force level is well captured by the simulation, but when the peak force is reached in the experiment, the force from the simulation continues to rise. The force drops gradually after the peak, and probably because we have neglected frictional effects, the force level drops faster and the impactor achieves complete perforation faster in the numerical simulation than in the experiment.

Even though the numerical results are acceptable in terms of ballistic limit velocity, Fig. 11 indicates that the numerical models have some shortcomings when it comes to describing the energy dissipation. The deflections at initial perforation are underestimated for both impactor shapes. The deflection values for the simulations with the ogival-ended impactor are most likely underestimated to some degree due to the use of element erosion. The deformation profiles are extracted from the state just after perforation which corresponds to the first state with eroded elements in the bottom plate.

### *6.3. Parametric study*

The mesh sensitivity of the problem is investigated briefly for both the blunt-ended and the ogival-ended impactors by creating models with twice as many elements over the plate thickness as the original models used in this study. This increased the simulation times considerably. In the case of the blunt-ended impactor, simulations were run with initial velocities of 5.9 m/s and 5.4 m/s. The respective residual velocities obtained with the original model are 3.9 m/s and 2.4 m/s, while the refined mesh yielded 4.1 m/s and 2.5 m/s. For the simulations with the ogival-ended impactor the initial velocities 5.0 m/s and 3.6 m/s were investigated. The respective residual velocities went from 3.8 m/s to 4.0 m/s and from 1.5 m/s to 1.9 m/s when the mesh was refined. Thus an increase in the residual velocities was seen for the refined meshes regardless of impactor shape, caused by an earlier occurence of failure. For both impactor shapes, the maximum force level dropped when the meshes were refined, and refining the grid size led to a force-time

curve slightly closer to the experimental results. However, the maximum force only went from 16.1 kN to 15.6 kN for the blunt-ended impactor and from 2.5 kN to 2.3 kN for the ogival-ended impactor.

By keeping the node spacing constant and changing the cubic 64-node hexahedrons to linear 8-node hexahedrons we get nine times as many elements in the model. This modification results in smaller deflections, i.e., less energy absorbed, and thus larger residual velocities. According to Fig. 11, the displacement field is generally underestimated from the numerical simulations suggesting that the cubic 64-node hexahedrons predict a more realistic response than the linear 8-node hexahedrons.

In the bulk of the simulations the frictional coefficient was set to zero. Simulations were run with $\mu = 0.05$ and $\mu = 0.1$ to assess the influence of friction on the numerical results. By increasing $\mu$, plastic strain and damage accumulate at the impactor-plate interface of the blunt-ended impactor. This resulted in earlier failure and lower capacity, contrasting the results from the simulations with the ogival-ended impactor where a higher $\mu$ led to a considerable reduction of the residual velocity of the impactor. The friction parameter is commonly set to zero or close to zero in ballistic analyses (see [21, 42–44]). Although investigations show that friction can be negligible in some cases [45], the frictional effect can influence the solution in other cases like in this study where the impact velocity is low. According to Rosenberg and Dekel [22] friction is still one of the less understood phenomena in terminal ballistics and they report that the friction present around the shank of a cylindrical projectile is small but not always insignificant. Kpenyigba et al. [5] investigated how lubricating the contact surface affects a conical projectile perforating a 1 mm thick steel plate, and the residual velocities reported did not change significantly with lubrication. In this study the numerical investigation on the effect of $\mu$ yielded inconclusive results, and the effect of friction was therefore disregarded.

The influence of the parameter $c$ controlling rate sensitivity in the thermoelastic-thermoviscoplastic model presented in Eq. (13) was investigated by comparing simulations with both impactor shapes for $c = 0$ and $c = 0.01$. Thermal softening, or the absense of such, was checked with adiabatic, isothermal, and thermally coupled formulations of the solver. The results in Table 7 show that introducing strain rate hardening increases the maximum force while it decreases the residual velocity as expected for both impactor shapes. Differences in the force level and residual velocity are generally small, but in the case of isothermal conditions the absence of thermal softening delays the onset of initial fracture for the plate struck by the blunt-ended impactor leading to a low residual velocity. This was also observed by Grytten et al. [20]. Comparing the results to the corresponding experiments shows that an isothermal formulation combined

with $c = 0.01$ gave the best results for the blunt-ended impactor. For the ogival-ended impactor the effect of temperature and strain-rate did not significantly change the results.

Measures were taken to ensure full clamping of the boundary in the experiments, and no deformation was seen around the bolted holes. However, studies have shown that the boundary behaves somewhere between fixed and simply supported, and that the effect of the boundaries increases as the impact velocity decreases [46]. In other words, as we approach quasi-static loading, more of the plate will be affected. The displacement profiles shown in Figs. 5 and 6 indicate that the entire plate is involved in the energy dissipation process for the blunt-ended impactor, but global deformation is less marked for the ogival-ended impacts. Simulations were therefore also run with simply supported boundaries. In the simulations with the blunt-ended impactor a simply supported formulation resulted in a lower residual velocity than a fixed boundary formulation. In the simulations using the ogival-ended impactor the residual velocitiy did not change noticeably for the simply supported simulation. The effect of boundary conditions on the residual velocity was found to be small in this study, so the conservative fixed boundary formulation has been chosen.

## 7. Concluding remarks

In this paper an experimental program concerning low-velocity impact on the dual-phase steel Docol 600DL was presented. The program includes material testing and calibration supported by DIC measurements, subsequent impact experiments in a dropped-objects-rig, and 3D finite element simulations. The bulk of the impact experiments were done on various layered configurations of 0.8 mm thick plates with a span of 300 mm. In addition, a smaller experimental program with 1.8 mm thick plates with the same span was carried out for comparison.

The impact experiments revealed that the thin plates' ability to resist perforation was greater when they were struck by a blunt-ended impactor than when they were struck by an ogival-ended impactor. This can be seen by comparing the ballistic limit velocities, which are higher when using the blunt-ended impactor. An almost linear relationship is found between the total plate thickness, i.e., number of layers, and the ballistic limit velocity for the respective impactors.

The blunt-ended impactor activates the entire plate in the energy dissipation process before the final failure happens in shear/plate thinning. On the other hand, plates struck with the ogival-ended impactor display a petaling fracture pattern, a significantly smaller global deformation, and less energy is absorbed by the plate, resulting in a lower ballistic limit. The failure mechanisms hardly vary when the plates are

laminated. The distinctive petaling pattern from the single plate struck by the ogival-ended impactor can be found in every plate in every configuration, the same being true for the bending, thinning, and shear failure caused by the blunt-ended impactor.

The same failure mechanisms from the 0.8 mm plates are observed in the impacts on the thicker 1.8 mm plates. However, the experimental results indicate that the energy absorption is higher for one thick monolithic plate than for layered plates of equal thickness. This is particularly clear for the ogival-ended impactor where the ballistic velocity and absorbed energy increased noticeably for the monolithic plate. Relating these findings to earlier research shows that layering might not be an advantageous strategy to improve the capacity of metallic plates subjected to low-velocity impact.

In the finite element simulations the behavior of the impacted plates in terms of plate thickness and layering was described with reasonable accuracy considering the complexity of the problem. This shows that a finite element model can predict failure modes and capture the trends present during low-velocity impact. That being said, the numerous mechanisms such as bending, membrane stretching, thinning, shear bands, and petaling, and uncertain factors like boundary conditions, thermal behavior, mesh sensitivity, friction, and strain rate make this low-velocity impact problem difficult to predict numerically.

**Acknowledgements**

The financial support for this work from the Norwegian Defence Estates Agency and the Structural Impact Laboratory (SIMLab), Centre for Research-based Innovation (CRI) at the Norwegian University of Science and Technology (NTNU) is gratefully acknowledged. The authors would also like to thank Dr. Egil Fagerholt for assistance with the DIC measurements.

## References


[1] Zukas JA. Impact Dynamics. John Wiley & Sons, Inc.; first ed.; 1982.

[2] Corbett GG, Reid SR, Johnson W. Impact loading of plates and shells by free-flying projectiles: A review. International Journal of Impact Engineering 1996;18:141–230.

[3] Backman ME, Goldsmith W. The mechanics of penetration of projectiles into targets. International Journal of Engineering Science 1978;16:1–99.

[4] Børvik T, Langseth M, Hopperstad OS, Malo KA. Perforation of 12 mm thick steel plates by 20 mm diameter projectiles with flat, hemispherical and conical noses. Part I: Experimental study. International Journal of Impact Engineering 2002;25:19–35.

[5] Kpenyigba KM, Jankowiak T, Rusinek A, Pesci R. Influence of projectile shape on dynamic behavior of steel sheet subjected to impact and perforation. Thin Walled Structures 2013;65:93–104.

[6] Iqbal MA, Gupta PK, Deore VS, Tak SK, Tiwari G, Gupta NK. Effect of target span and configuration on the ballistic limit. International Journal of Impact Engineering 2012;42:11–24.

[7] Gupta NK, Iqbal MA, Sekhon GS. Experimental and numerical studies on the behavior of thin aluminum plates subjected to impact by blunt- and hemispherical-nosed projectiles. International Journal of Impact Engineering 2006;32:1921–44.

[8] Gupta NK, Iqbal MA, Sekhon GS. Effect of projectile nose shape, impact velocity and target thickness on the deformation behavior of layered plates. International Journal of Impact Engineering 2006;32:37–60.

[9] Woodward RL, Cimpoeru SJ. A study of the perforation of aluminium laminate targets. International Journal of Impact Engineering 1998;21:117–31.

[10] Dey S, Børvik T, Teng X, Wierzbicki T, Hopperstad OS. On the ballistic resistance of double-layered steel plates: An experimental and numerical investigation. International Journal of Solids and Structures 2007;44:6701–23.

[11] Ben-Dor G, Dubinsky A, Elperin T. Investigation and optimization of protective properties of metal multi-layered shields: A review. International Journal of Protective Structures 2012;3:275–91.

[12] Langseth M, Larsen PK. Dropped objects' plugging capacity of steel plates: An experimental investigation. International Journal of Impact Engineering 1990;9:289–316.

[13] Wen HM, Jones N. Low-velocity perforation of punch-impact-loaded metal plates. Journal of Pressure Vessel Technology, Transactions of the ASME 1996;118:181–7.

[14] Mohotti D, Muneeb A, Ngo T, Lu J, Mendis P, Ruan D. Out-of-plane impact resistance of aluminium plates subjected to low velocity impact. Materials and Design 2013;50:413–26.

[15] Abdulhamid H, Kolopp A, Bouvet C, Rivallant S. Experimental and numerical study of AA5086-H111 aluminum plates subjected to impact. International Journal of Impact Engineering 2013;51:1–12.

[16] Rusinek A, Rodriguez-Martinez JA, Zaera R, Klepaczko JR, Arias A, Sauvelet C. Experimental and numerical study of the perforation process of mild steel sheets subjected to perpendicular impact by hemispherical projectiles. International Journal of Impact Engineering 2009;36:565–87.

[17] SSAB EMEA AB, SE-781 84 Borlange, Sweden . Datasheet 13-02-14 GB8201 DOCOL; Cited 2014-03-20. http://www.ssab.com/en/Brands/Docol1/Products/Docol-600-DL/.

[18] Fagerholt E, Børvik T, Hopperstad OS. Measuring discontinuous displacement fields in cracked specimens using digital image correlation with mesh adaptation and crack-path optimization. Optics and Lasers in Engineering 2013;51:229–310.

[19] Gruben G, Fagerholt E, Hopperstad OS, Børvik T. Fracture characteristics of a cold-rolled dual-phase steel. European Journal of Mechanics - A/Solids 2011;30:204 –18.

[20] Grytten F, Børvik T, Hopperstad OS, Langseth M. Low velocity perforation of AA5083-H116 aluminium plates. International Journal of Impact Engineering 2009;36:597–610.

[21] Børvik T, Langseth M, Hopperstad OS, Malo KA. Ballistic penetration of steel plates. International Journal of Impact Engineering 1999;22:855–86.

[22] Rosenberg Z, Dekel E. Terminal Ballistics. Springer-Verlag Berlin Heidenberg; 2012.

[23] Børvik T, Hopperstad OS, Pedersen KO. Quasi-brittle fracture during structural impact of AA7075-T651 aluminium plates. International Journal of Impact Engineering 2010;37:537–51.

[24] CEAST 9350 Instructions for use and maintenance. Instron; first ed.; 2010.

[25] Gruben G. Private communication. 2014.

[26] Gruben G, Vysochinskiy D, Coudert T, Reyes A, Lademo OG. Determination of ductile fracture parameters of a dual-phase steel by optical measurements. Strain 2013;49:221–32.

[27] Recht RF, Ipson TW. Ballistic perforation dynamics. Journal of Applied Mechanics 1963;30:384–90.

[28] Langseth M, Larsen PK. Dropped objects' plugging capacity of aluminium alloy plates. International Journal of Impact Engineering 1994;15:225–41.

[29] Wierzbicki T. Petalling of plates under explosive and impact loading. International Journal of Impact Engineering 1999;22:935–54.

[30] Lee YW, Wierzbicki T. Fracture prediction of thin plates under localized impulsive loading. Part I: Dishing. International Journal of Impact Engineering 2005;31:1253–76.

[31] Lee YW, Wierzbicki T. Fracture prediction of thin plates under localized impulsive loading. Part II: Discing and petalling. International Journal of Impact Engineering 2005;31:1277–308.

[32] Rosenberg Z, Dekel E. On the deep penetration and plate perforation by rigid projectiles. International Journal of Solid and Structures 2009;46:4169–80.

[33] Børvik T, Hopperstad OS, Berstad T, Langseth M. A computational model of viscoplasticity and ductile damage for impact and penetration. European Journal of Mechanics A/Solids 2001;20:685–712.

[34] Cockcroft MG, Latham DJ. Ductility and the workability of metals. Journal of the Institute of Metals 1968;96:33–9.

[35] Dey S, Børvik T, Hopperstad OS, Langseth M. On the influence of fracture criterion in projectile impact of steel plates. Computational Materials Science 2006;38:176–91.

[36] Kane, A. and Børvik, T. and Berstad, T. and Benallal, A. and Hopperstad, O. S. . Failure criteria with unilateral conditions for simulation of plate perforation. European Journal of Mechanics - A/Solids 2011;30:468–76.

[37] Børvik T, Dey S, Clausen AH. Perforation resistance of five different high-strength steel plates subjected to small-arms projectiles. International Journal of Impact Engineering 2009;36:948–64.

[38] Rakvåg KG, Underwood NJ, Schleyer GK, Børvik T, Hopperstad OS. Transient pressure loading of clamped metallic plates with pre-formed holes. International Journal of Impact Engineering 2013;53:44–55.

[39] LSTC. LS-DYNA; Cited 2014-20-01. http://www.lstc.com/products/ls-dyna.

[40] LSTC. LS-OPT; Cited 2014-20-01. http://www.lstc.com/products/ls-opt.

[41] IMPETUS Afea AS . IMPETUS Afea Solver; Cited 2014-20-01. http://www.impetus-afea.com.

[42] Holmen JK, Johnsen J, Jupp S, Hopperstad OS, Børvik T. Effects of heat treatment on the ballistic properties of AA6070 aluminium alloy. International Journal of Impact Engineering 2013;57:119–33.

[43] Johnsen J, Holmen JK, Myhr OR, Hopperstad OS, Børvik T. A nano-scale material model applied in finite element analysis of aluminium plates under impact loading. Computational Materials Science 2013;79:724–35.

[44] Arias A, Rodriguez-Martinez JA, Rusinek A. Numerical simulations of impact behaviour of thin steel plates subjected to cylindrical, conical and hemispherical non-deformable projectiles. Engineering Fracture Mechanics 2008;75:1635–56.

[45] Børvik T, Olovsson L, Dey S, Langseth M. Normal and oblique impact of small arms bullets on AA6082-T4 aluminium protective plates. International Journal of Impact Engineering 2011;38:577–89.

[46] Grytten F, Fagerholt E, Auestad T, Førre B, Børvik T. Out-of-plane deformation measurements of an aluminium plate during quasi-static perforation using structured light and close-range photogrammetry. International Journal of Solids and Structures 2007;44:5752–73.

## Tables and figures

Table 1: Nominal chemical composition of Docol 600DL steel in wt-% [17].

| C | Si | Mn | P | S | $Al_{tot}$ | Fe |
|---|---|---|---|---|---|---|
| 0.10 | 0.40 | 1.50 | 0.010 | 0.002 | 0.040 | Balance |

Table 2: Number of impact experiments conducted in this study as a function of impactor shape, plate thickness and layer configuration.

| Plate | Blunt-ended | | | | Ogival-ended | | | |
|---|---|---|---|---|---|---|---|---|
| thickness | 1 plate | 2 plates | 3 plate | 4 plates | 1 plate | 2 plates | 3 plate | 4 plates |
| 0.8 mm | 4 | 4 | 5 | 4 | 4 | 4 | 4 | 4 |
| 1.8 mm | 4 | 1 | - | - | 6 | 1 | - | - |

Table 3: Ballistic limit velocities, $v_{bl}$, and the parameters, $a$ and $p$, of the Lambert equation for the various plate configurations involving 0.8 mm Docol 600DL plates.

| Impactor shape | No. of layers | Experimental data | | | Numerical simulations | | | Deviation |
|---|---|---|---|---|---|---|---|---|
| | | $v_{bl}$ (m/s) | $a$ | $p$ | $v_{bl}$ (m/s) | $a$ | $p$ | $\Delta v_{bl}$ (m/s) |
| Blunt-ended | 1 | 5.3 | 0.96 | 2.43 | 4.7 | 0.89 | 2.24 | -0.6 |
| | 2 | 8.1 | 1.00 | 2.57 | 6.5 | 0.99 | 2.04 | -1.6 |
| | 3 | 9.8 | 0.83 | 2.98 | 7.9 | 0.93 | 2.04 | -1.9 |
| | 4 | 12.0 | 0.82 | 2.91 | 9.2 | 0.97 | 2.05 | -2.8 |
| Ogival-ended | 1 | 2.6 | 1.00 | 1.63 | 3.3 | 1.00 | 1.97 | 0.7 |
| | 2 | 5.0 | 1.00 | 1.86 | 5.0 | 1.00 | 2.00 | 0.0 |
| | 3 | 6.4 | 1.00 | 1.70 | 6.4 | 1.00 | 2.00 | 0.0 |
| | 4 | 9.0 | 1.00 | 1.88 | 7.9 | 1.00 | 2.02 | -1.1 |

Table 4: Ballistic limit velocities, $v_{bl}$, and the parameters, $a$ and $p$, of the Lambert equation for the various plate configurations involving 1.8 mm Docol 600DL plates.

| Impactor shape | No. of layers | Experimental data | | | Numerical simulations | | | Deviation |
|---|---|---|---|---|---|---|---|---|
| | | $v_{bl}$ (m/s) | $a$ | $p$ | $v_{bl}$ (m/s) | $a$ | $p$ | $\Delta v_{bl}$ (m/s) |
| Blunt-ended | 1 | 8.9 | 1.00 | 2.37 | 7.8 | 1.00 | 2.27 | -1.2 |
| | 2 | 12.7 | 1.00 | 2.00 | 10.5 | 1.00 | 2.00 | -2.2 |
| Ogival-ended | 1 | 6.7 | 1.00 | 2.05 | 6.8 | 1.00 | 1.93 | 0.1 |
| | 2 | 11.7 | 1.00 | 2.00 | 10.5 | 1.00 | 2.00 | -1.2 |

Table 5: Calibrated material parameters for the extended Voce hardening rule and CL criterion.

| $\sigma_0$ (MPa) | $Q_1$ (MPa) | $C_1$ | $Q_2$ (MPa) | $C_2$ | $W_{cr}$ (MPa) |
|---|---|---|---|---|---|
| 370.0 | 236.4 | 39.3 | 408.1 | 4.5 | 473.0 |

Table 6: Physical constants and model parameters for the Docol 600DL steel plates taken from the literature [33, 37, 38].

| $E$ (MPa) | $\nu$ (-) | $\rho$ (kg/m$^3$) | $\alpha$ (K$^{-1}$) | $C_p$ (J/(kg K)) | $\dot{p}_0$ (s$^{-1}$) | $c$ (-) | $\chi$ (-) | $k$ (W/(m K)) | $T_0$ (K) | $T_m$ (K) | $m$ (-) |
|---|---|---|---|---|---|---|---|---|---|---|---|
| 210,000 | 0.33 | 7850 | $1.2 \times 10^{-5}$ | 452 | $5 \times 10^{-4}$ | 0.01 | 0.9 | 50 | 293 | 1800 | 1 |

Table 7: Summary of how temperature and strain rate affect the numerical simulations of the perforation process for impact on single plates. The residual velocity ($v_r$), peak force ($F_{peak}$), and the energy absorption ($W$) defined in Eq. (3) are given for each simulation.

| | Blunt-ended impactor ($v_i$ = 5.9 m/s) | | Ogival-ended impactor ($v_i$ = 3.6 m/s) | |
|---|---|---|---|---|
| | Rate sensitive ($c$ = 0.01) | Rate insensitive ($c$ = 0) | Rate sensitive ($c$ = 0.01) | Rate insensitive ($c$ = 0) |
| Adiabatic | $v_r$ = 3.9 m/s<br>$F_{peak}$ = 16.2 kN<br>$W$ = 95.9 J | $v_r$ = 4.2 m/s<br>$F_{peak}$ = 14.0 kN<br>$W$ = 84.3 J | $v_r$ = 1.5 m/s<br>$F_{peak}$ = 2.4 kN<br>$W$ = 51.9 J | $v_r$ = 1.6 m/s<br>$F_{peak}$ = 2.3 kN<br>$W$ = 49.5 J |
| Coupled | $v_r$ = 3.9 m/s<br>$F_{peak}$ = 16.3 kN<br>$W$ = 96.9 J | $v_r$ = 4.2 m/s<br>$F_{peak}$ = 14.0 kN<br>$W$ = 84.7 J | $v_r$ = 1.5 m/s<br>$F_{peak}$ = 2.4 kN<br>$W$ = 52.0 J | $v_r$ = 1.6 m/s<br>$F_{peak}$ = 2.4 kN<br>$W$ = 50.1 J |
| Isothermal | $v_r$ = 2.7 m/s<br>$F_{peak}$ = 17.4 kN<br>$W$ = 134.9 J | $v_r$ = 4.0 m/s<br>$F_{peak}$ = 15.2 kN<br>$W$ = 92.4 J | $v_r$ = 1.5 m/s<br>$F_{peak}$ = 2.4 kN<br>$W$ = 51.0 J | $v_r$ = 1.6 m/s<br>$F_{peak}$ = 2.3 kN<br>$W$ = 49.8 J |

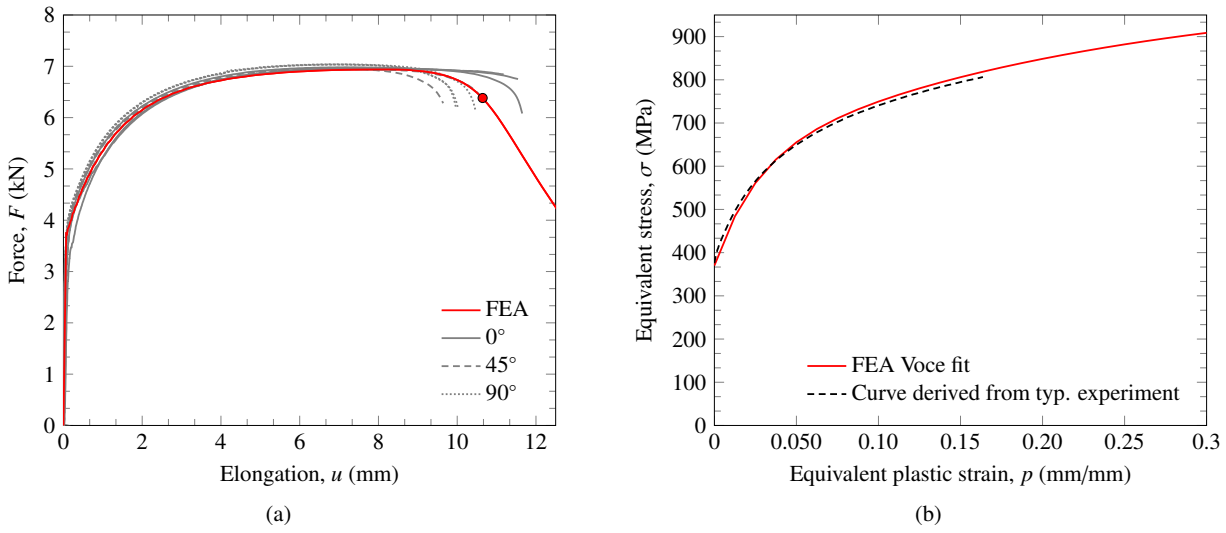


Figure 1: (a) Force-elongation curves from DIC-measurements with 40 mm initial gauge-length and the corresponding finite element solution. The circle denotes the assumed point of fracture in the calculation of $W_{cr}$. (b) Equivalent stress-equivalent plastic strain curves for the representative uniaxial tensile test (until necking), and the optimized extended Voce hardening rule with parameters shown in Table 5.

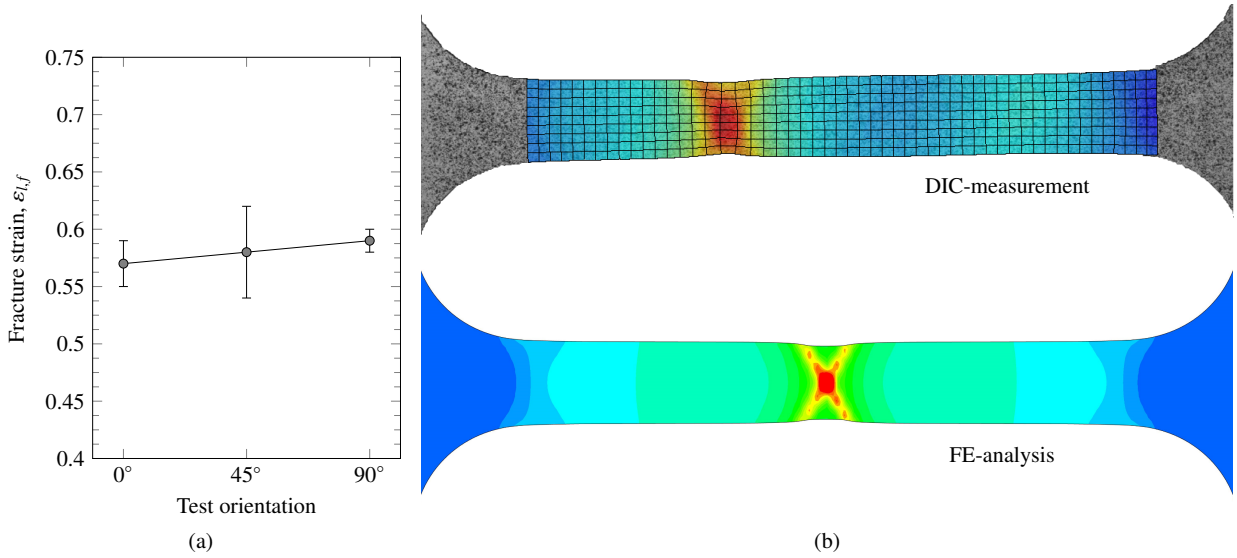


Figure 2: (a) The logarithmic surface strain at incipient fracture $\varepsilon_{l,f}$ taken from DIC measurements for the three different directions. (b) Comparison of the surface strain in a DIC measurement and a corresponding finite element model of a tensile test at incipient fracture. The fringes are in the range from 0 (blue) to 0.5 (red).

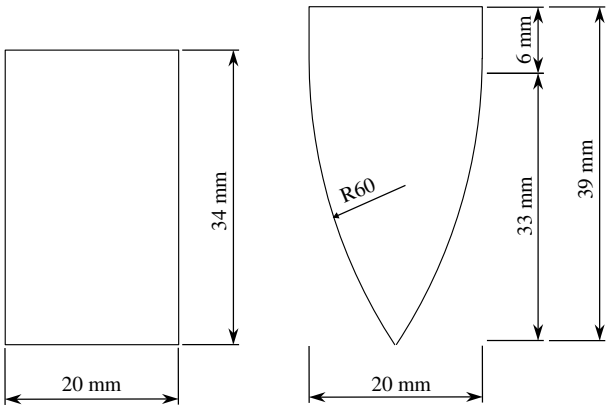


Figure 3: Geometry of the impactors. The ogival-ended impactor has a caliber radius head (CRH) of 3.

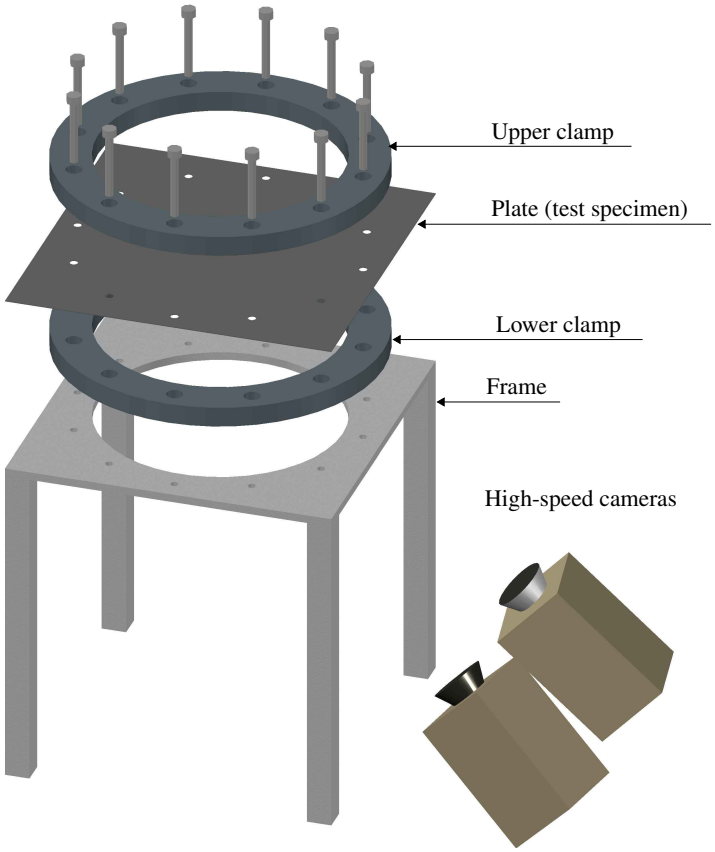


Figure 4: Illustration of the test set-up and camera placement.

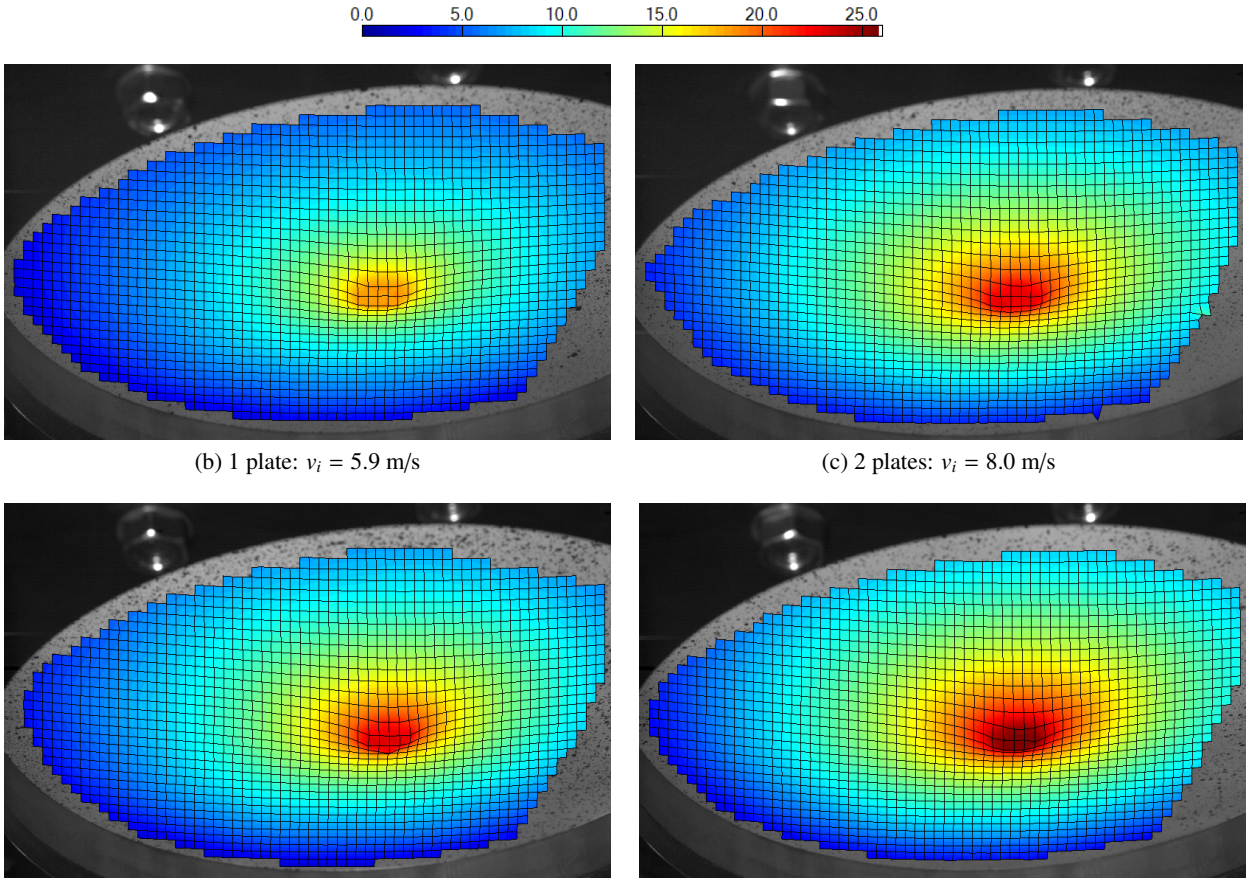


(b) 1 plate: $v_i$ = 5.9 m/s

(c) 2 plates: $v_i$ = 8.0 m/s

(d) 3 plates: $v_i$ = 12.0 m/s

(e) 4 plates: $v_i$ = 14.0 m/s

Figure 5: Deformation profiles based on DIC-measurements just before perforation from tests with the blunt-ended impactor: (a) 1 plate, (b) 2 plates, (c) 3 plates, and (d) 4 plates. Fringe values are given in mm.

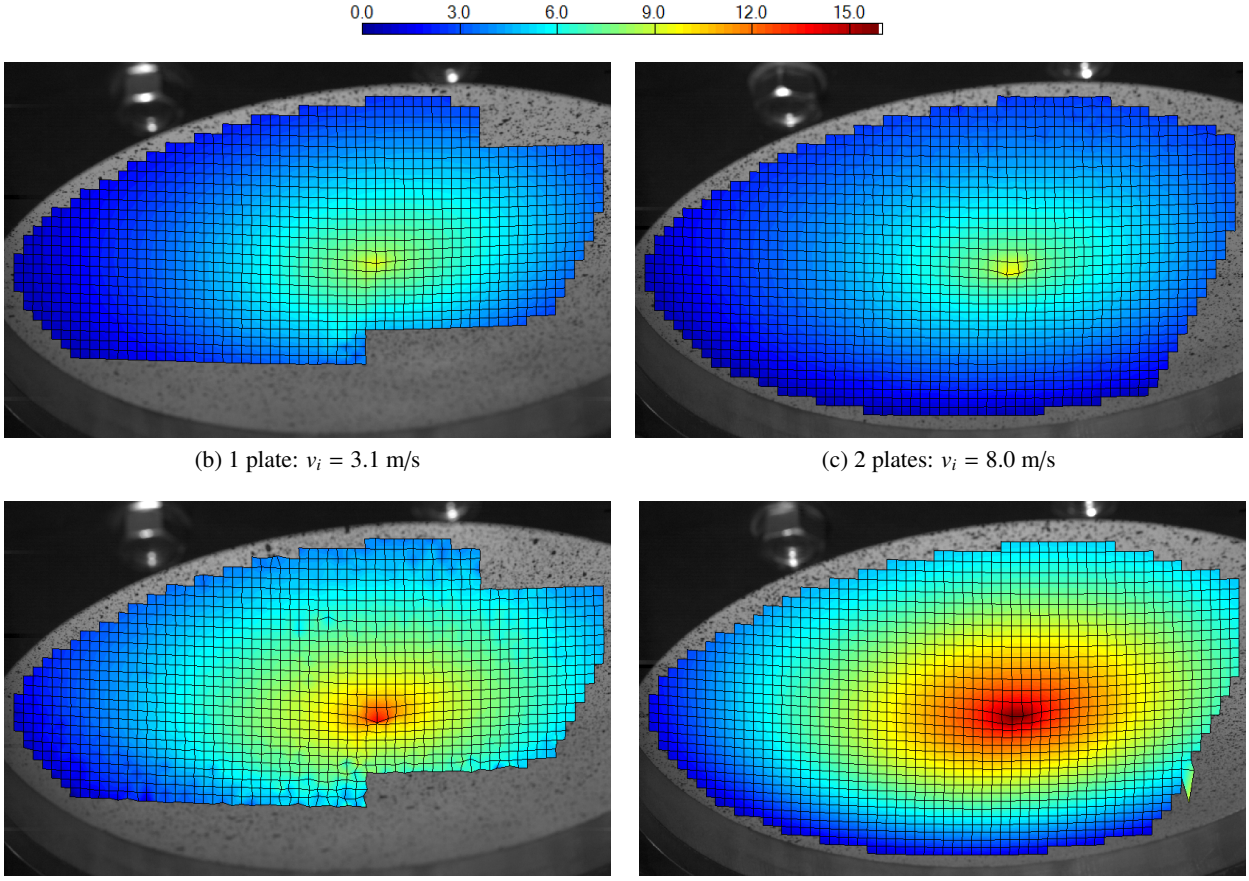


(b) 1 plate: $v_i$ = 3.1 m/s

(c) 2 plates: $v_i$ = 8.0 m/s

(d) 3 plates: $v_i$ = 10.0 m/s

(e) 4 plates: $v_i$ = 14.0 m/s

Figure 6: Deformation profiles based on DIC-measurements just before perforation from tests with the ogival-ended impactor: (a) 1 plate, (b) 2 plates, (c) 3 plates, and (d) 4 plates. Fringe values are given in mm.

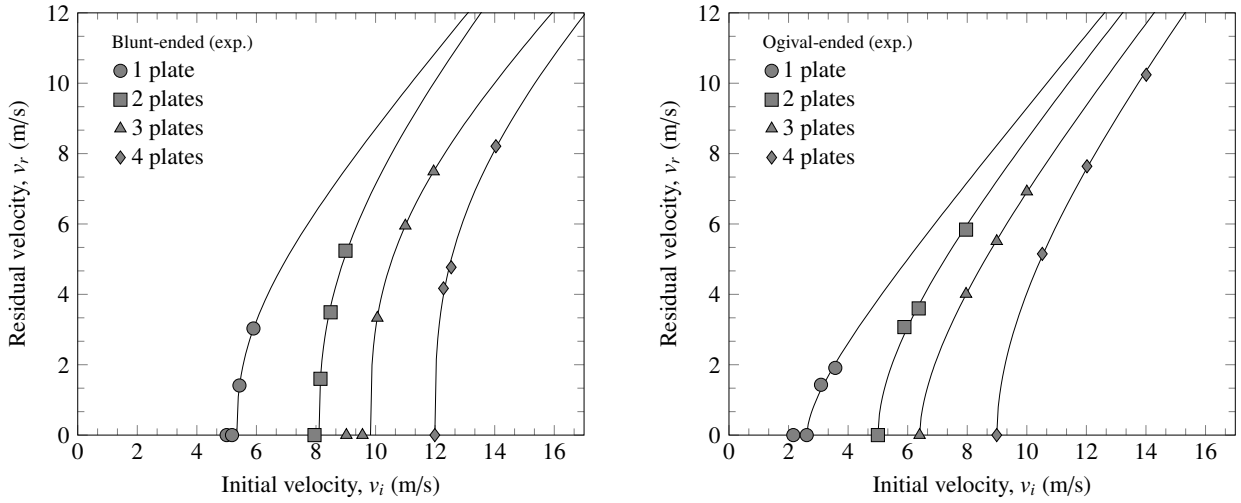


(a) Experimental values, blunt-ended impactor




(b) Experimental values, ogival-ended impactor

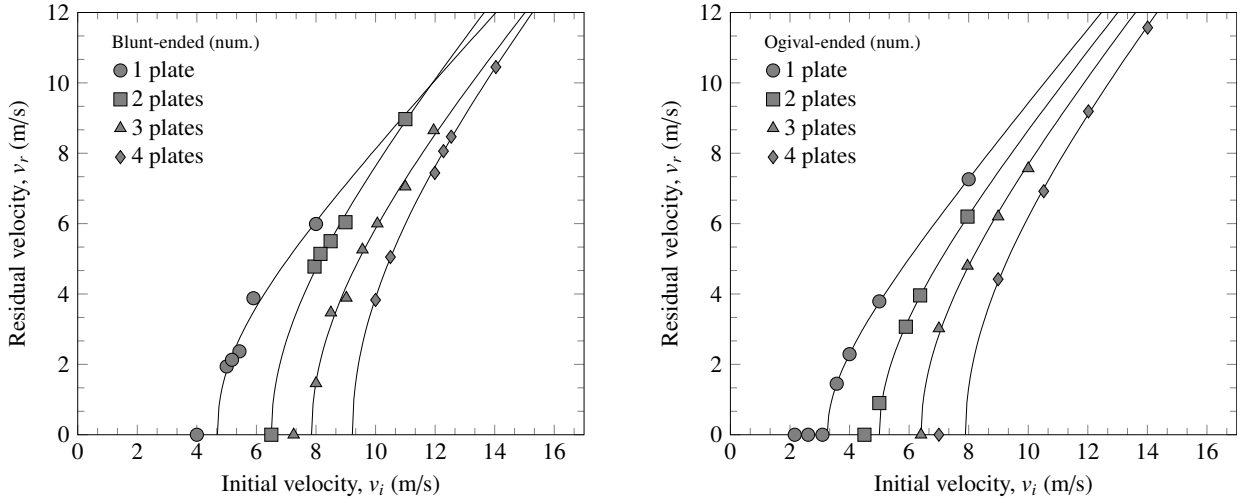


(c) Simulated values, blunt-ended impactor




(d) Simulated values, ogival-ended impactor

Figure 7: Ballistic curves from experimental tests with (a) the blunt-ended impactor and (b) the ogival-ended impactor; and ballistic curves from finite element simulations with (c) the blunt-ended impactor (d) the ogival-ended impactor.

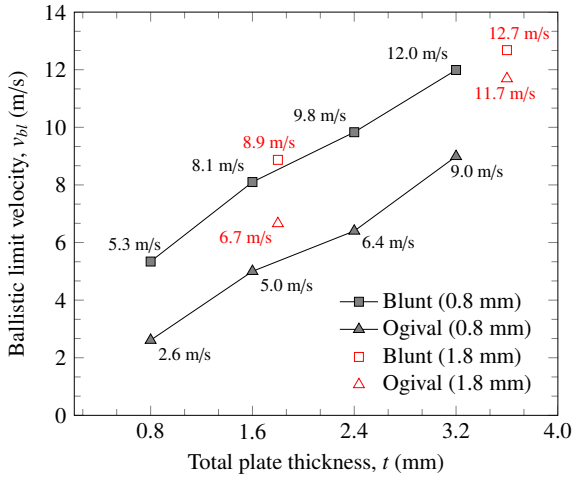


(a) Experimental tests

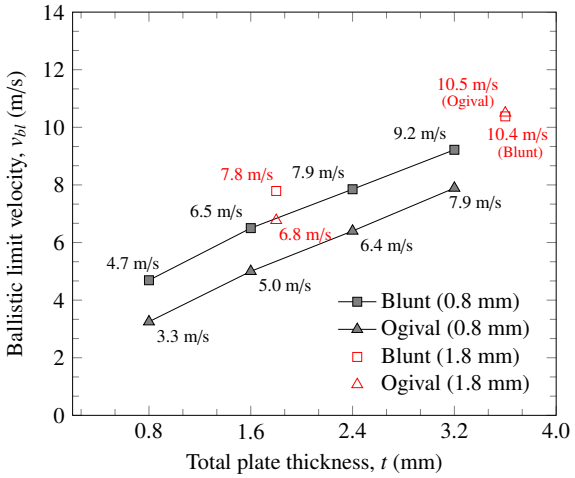


(b) Numerical simulations

Figure 8: Ballistic limit velocities from all plate-impactor combinations as a function of the total plate thickness found from (a) the experimental tests and (b) the numerical simulations.

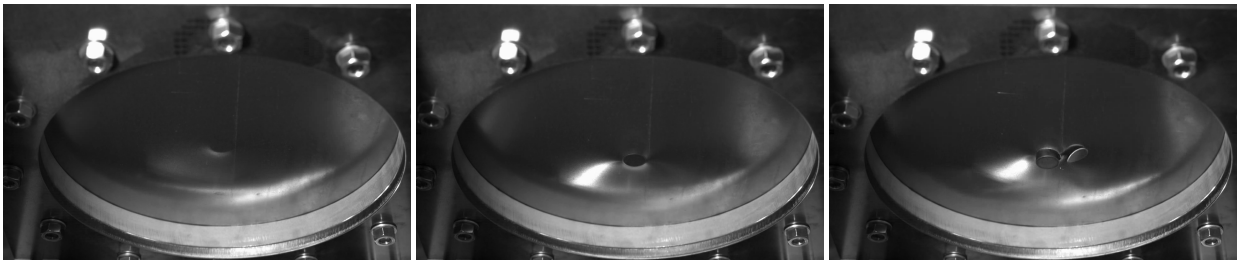

(a) Perforation by a blunt-ended impactor ($v_i$ = 5.9 m/s, $v_r$ = 3.0 m/s).

(b) Petal formation during perforation by an ogival-ended impactor ($v_i$ = 3.6 m/s, $v_r$ = 1.9 m/s).

Figure 9: Timelapses showing perforation of a single 0.8 mm plate by (a) the blunt-ended impactor and (b) the ogival-ended impactor.

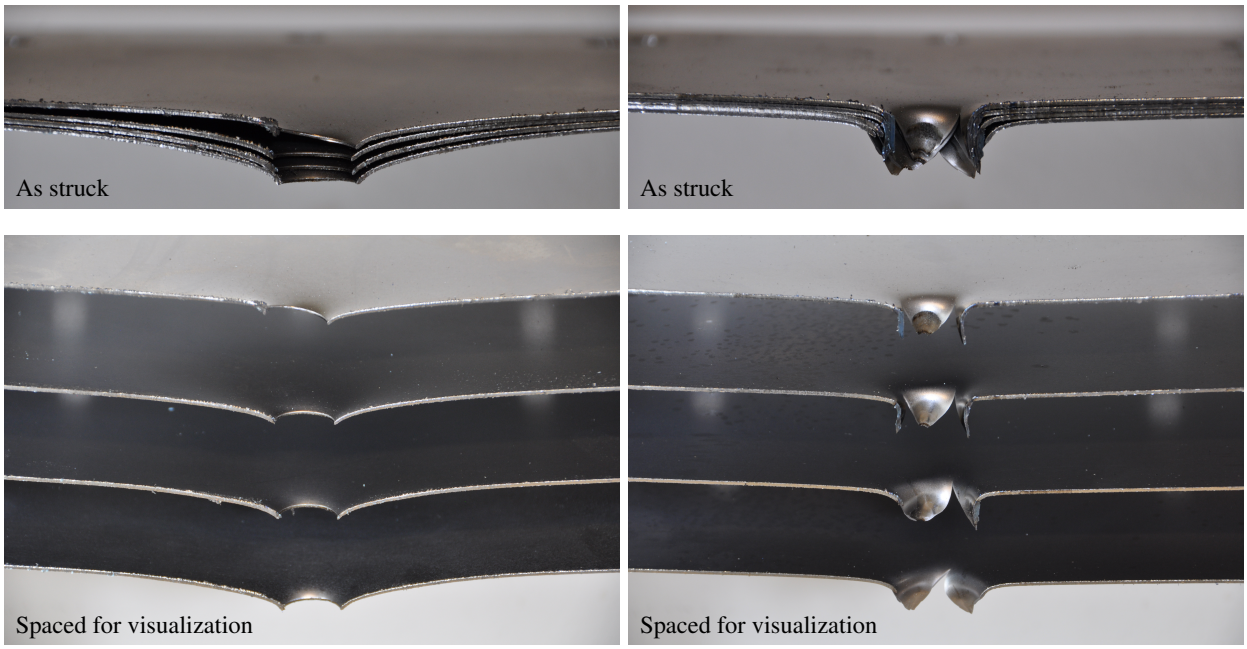


(a) Blunt-ended impactor ($v_i$ = 14.0 m/s, $v_r$ = 8.2 m/s)

(b) Ogival-ended impactor ($v_i$ = 10.5 m/s, $v_r$ = 5.2 m/s)

Figure 10: Post perforation pictures of 0.8 mm quadruple-layered plates: (a) shows plates struck by the blunt-ended impactor while (b) shows plates struck by the ogival-ended impactor. The bottom pictures show the plates with spacing to better illustrate the failure process.

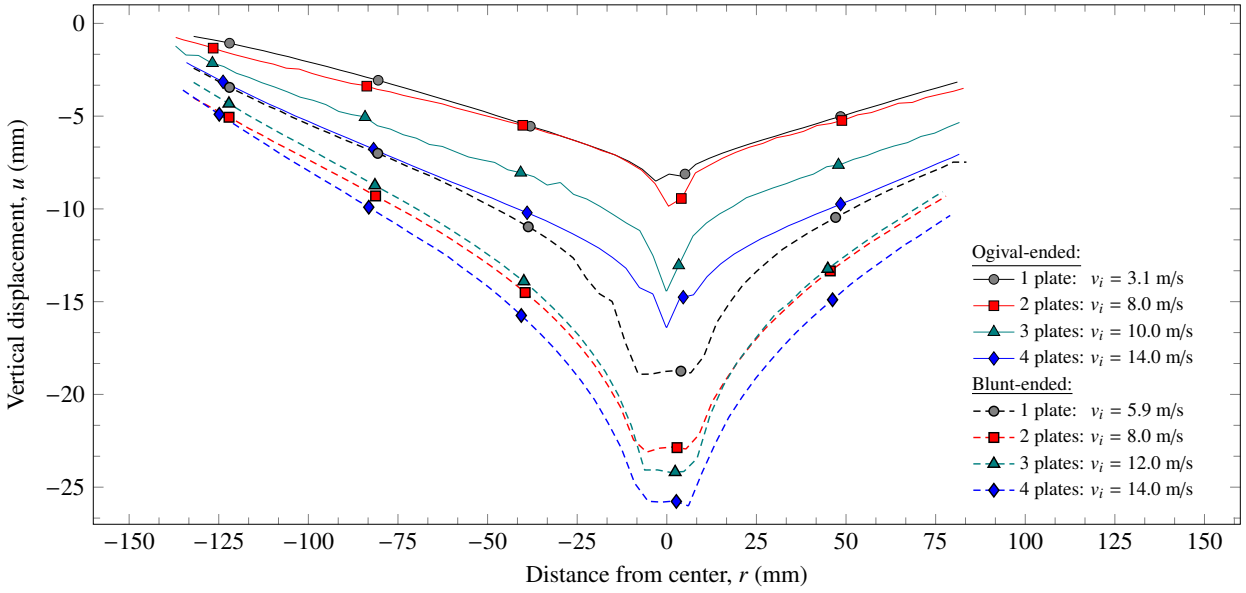


(a) Experimental tests

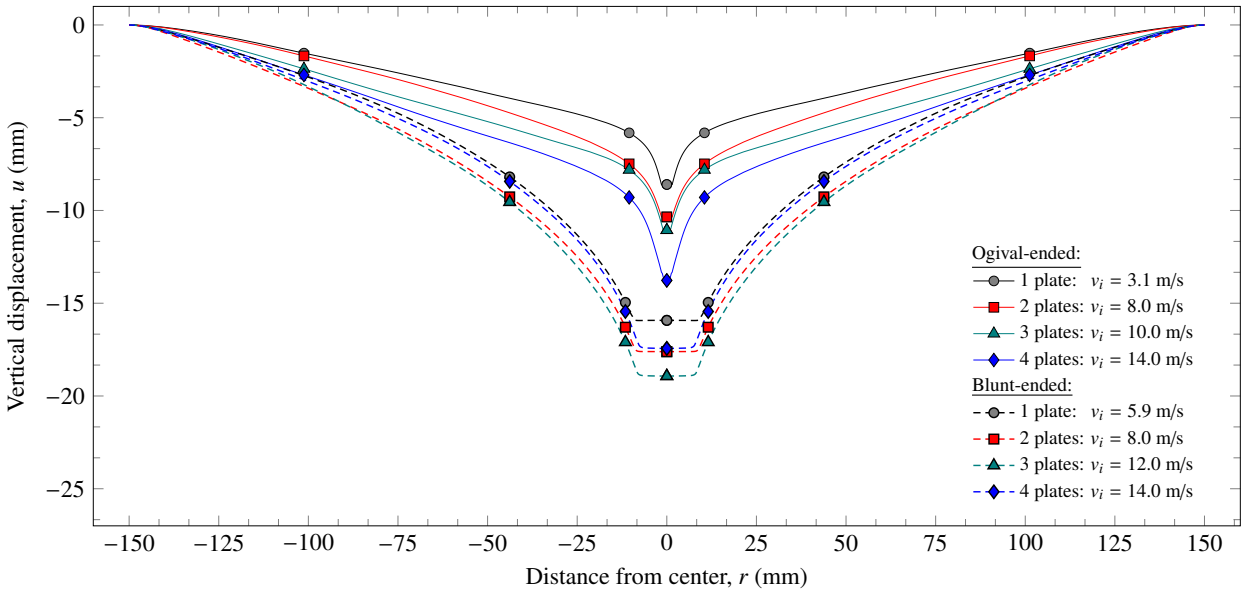


(b) Numerical simulations

Figure 11: Deflection profiles extracted just before failure for a selection of experiments: (a) DIC-based from experiments, (b) from the finite element simulations.

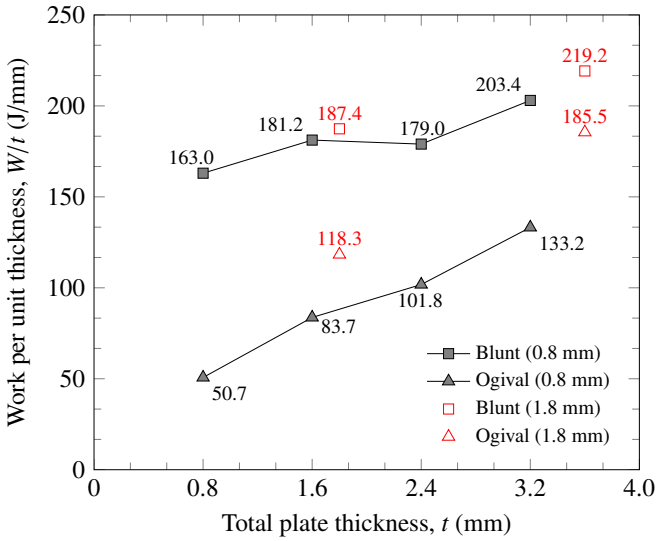


Figure 12: Average work per unit thickness ($W/t$) for the different plate-projectile configurations.

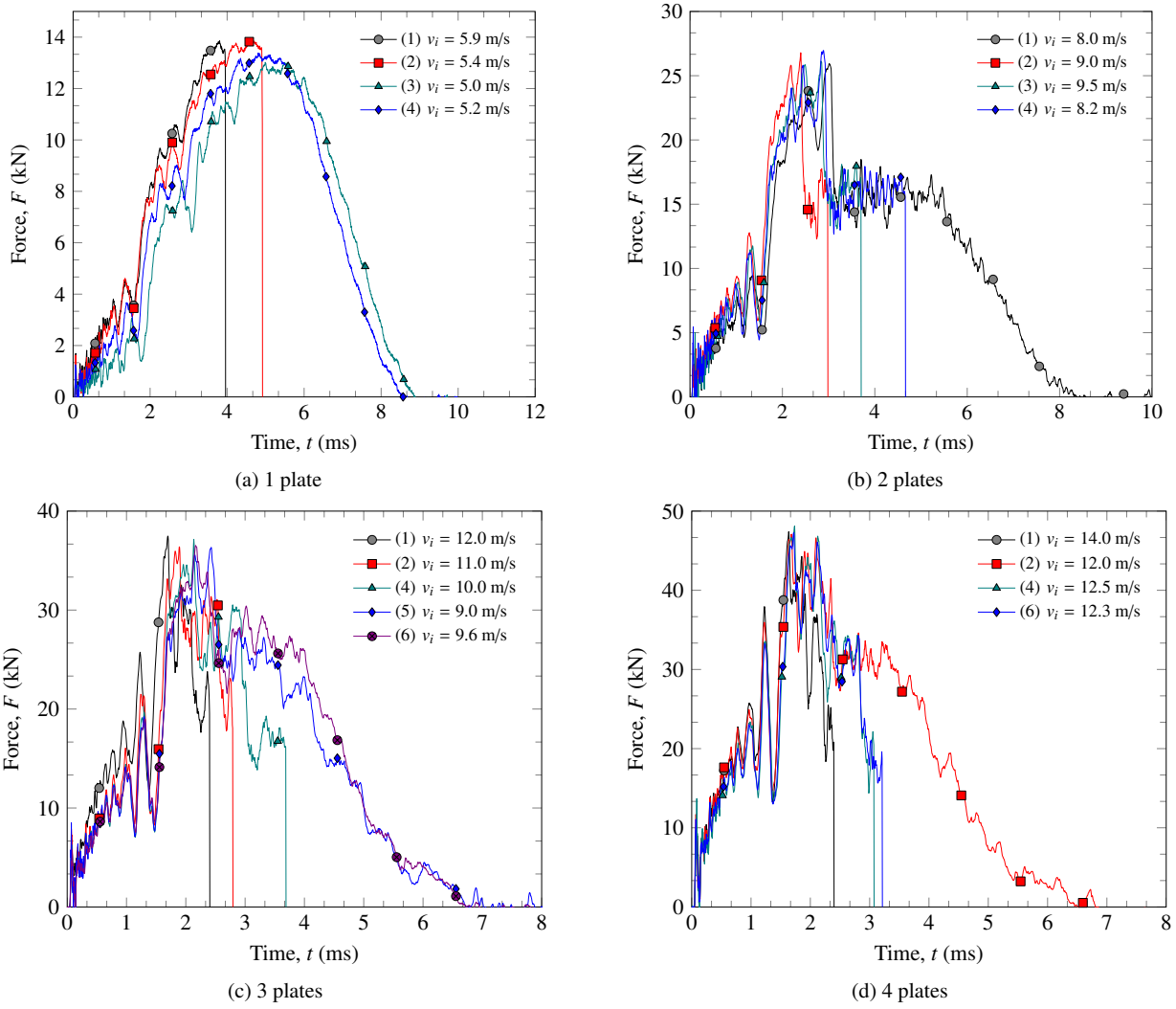


(a) 1 plate

(b) 2 plates

(c) 3 plates

(d) 4 plates

Figure 13: Force-time curves for experiments carried out with the blunt-ended impactor: (a), (b), (c) and (d) show curves for 1, 2, 3 and 4 plates respectively.

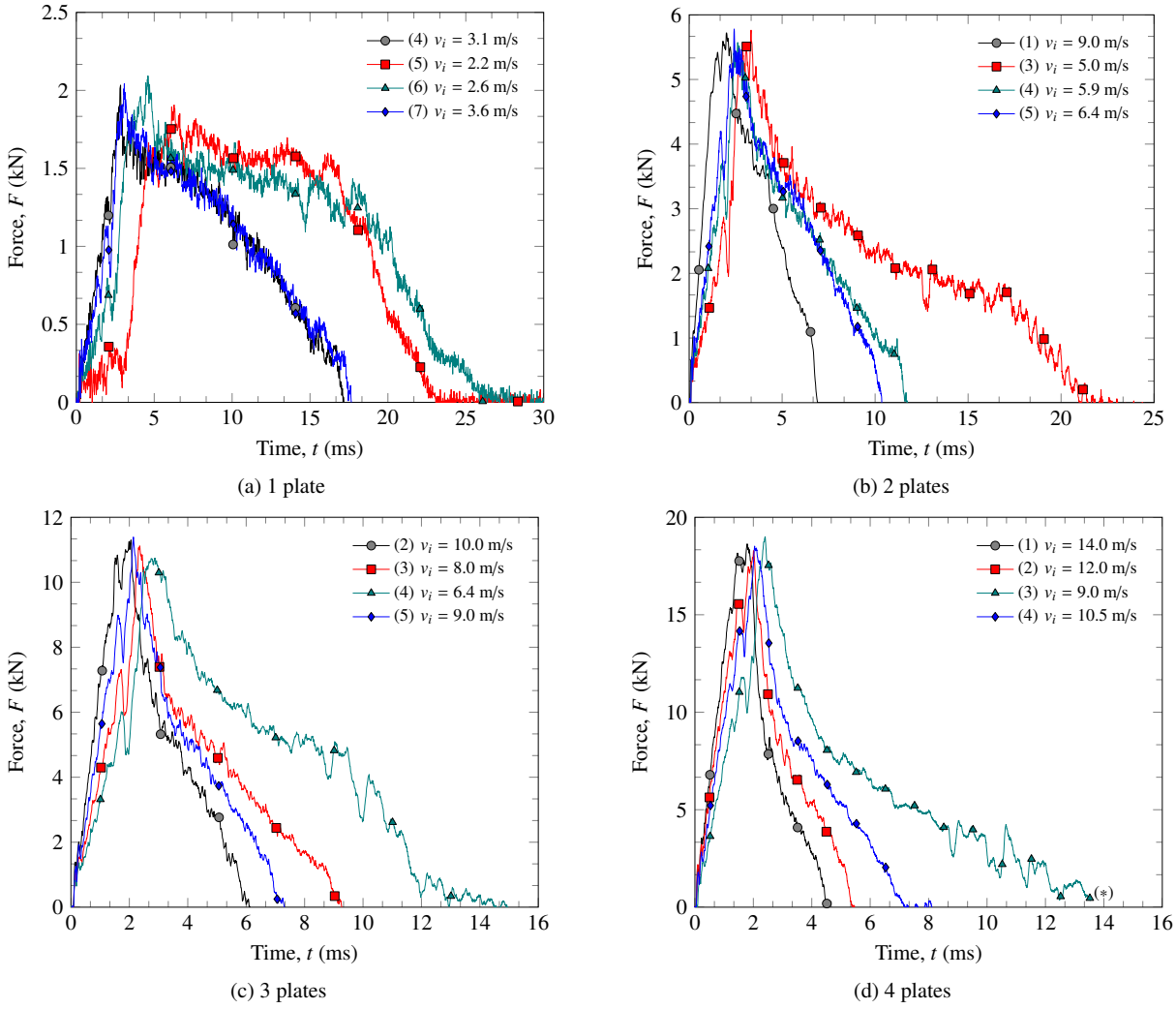


Figure 14: Force-time curves for experiments carried out with the ogival-ended impactor: (a), (b), (c) and (d) show curves for 1, 2, 3 and 4 plates respectively. (∗) This test did not perforate the plate, however, not enough data was acquired to plot the entire curve.

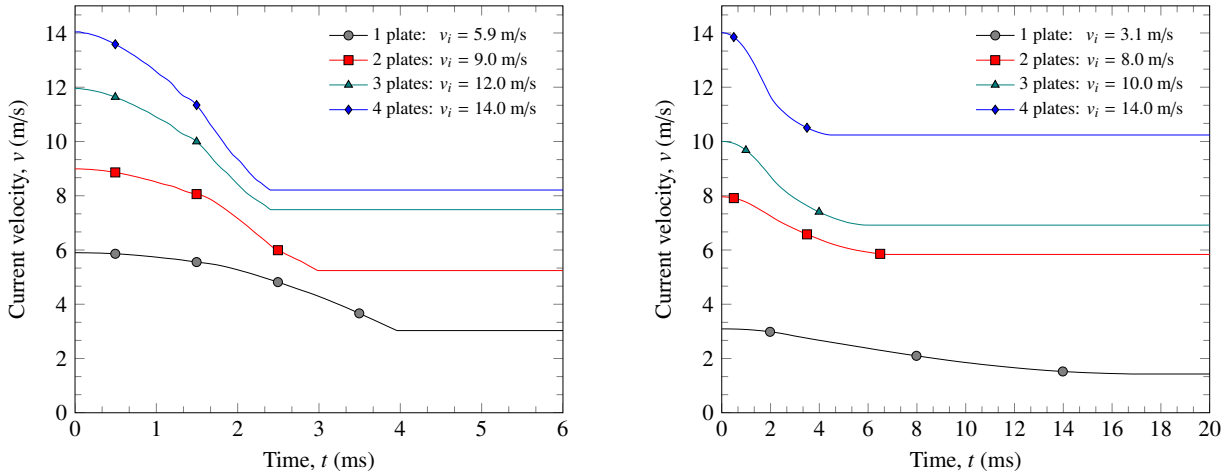


(a) Blunt-ended impactor

(b) Ogival-ended impactor

Figure 15: Typical experimental velocity-time curves for (a) tests with the blunt-ended impactor and (b) tests with the ogival-ended impactor.

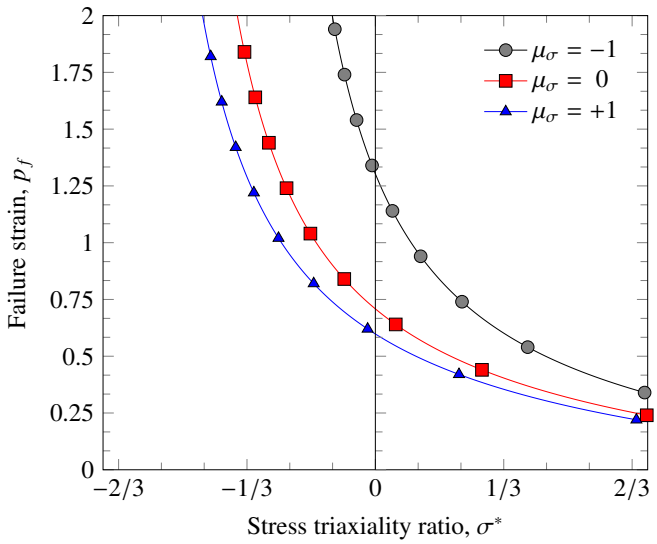


Figure 16: Influence of the Lode parameter $\mu_\sigma$ and the stress triaxiality ratio $\sigma^*$ on the failure strain for the failure parameter $W_{cr}$ = 473 MPa used in this study.

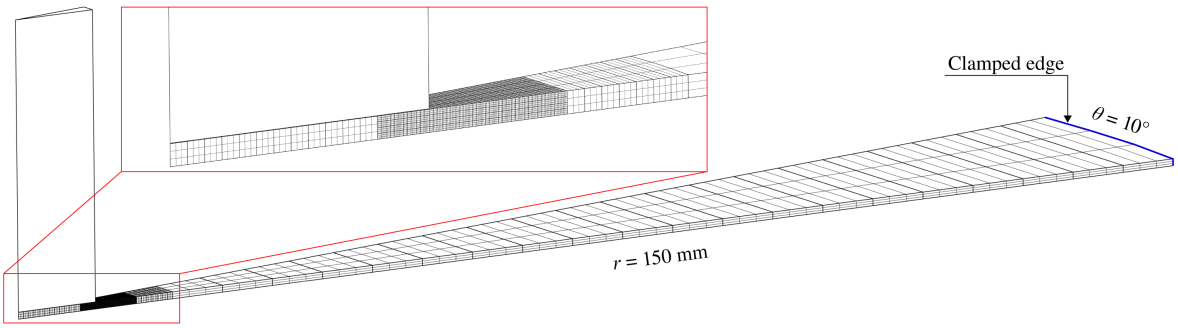


(a) Blunt-ended impactor

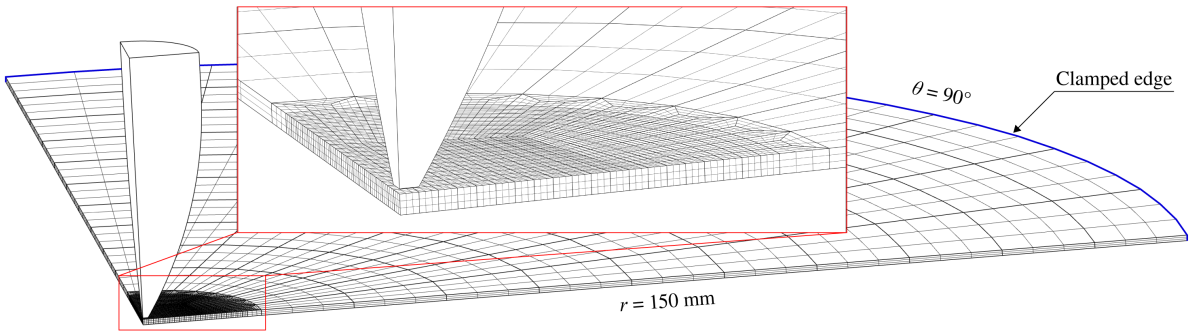


(b) Ogival-ended impactor

Figure 17: Meshes applied in the IMPETUS Afea Solver for the 0.8 mm plates.

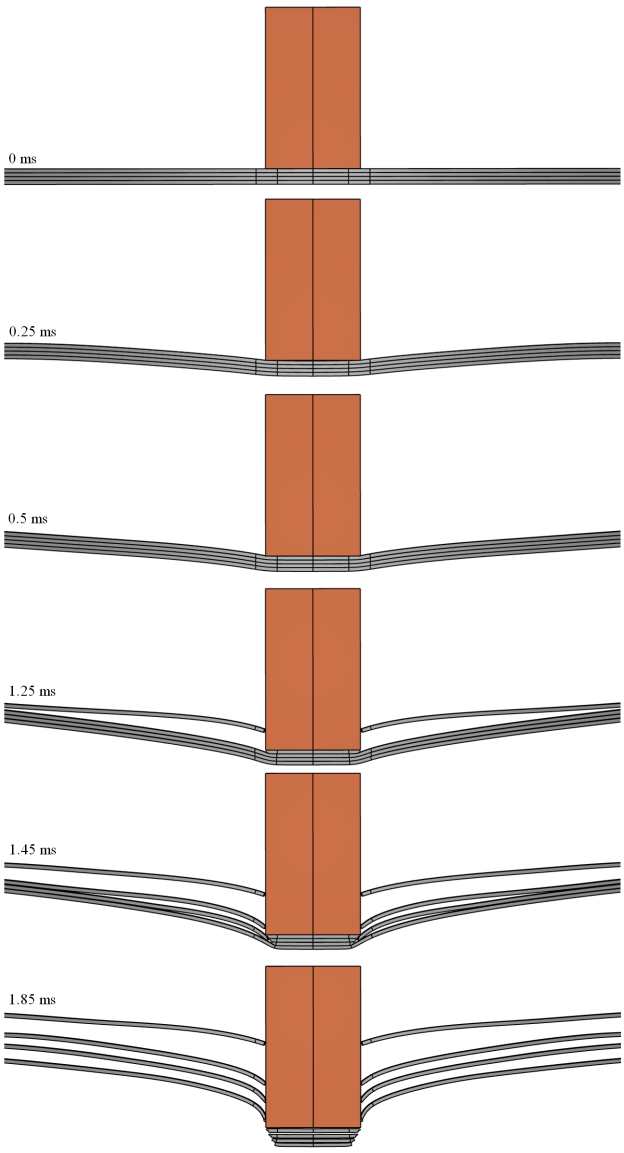


Figure 18: Image series displaying the predicted perforation process of a 4 plates by the blunt-ended impactor ($v_i$ = 14.0 m/s, $v_r$ = 10.5 m/s).

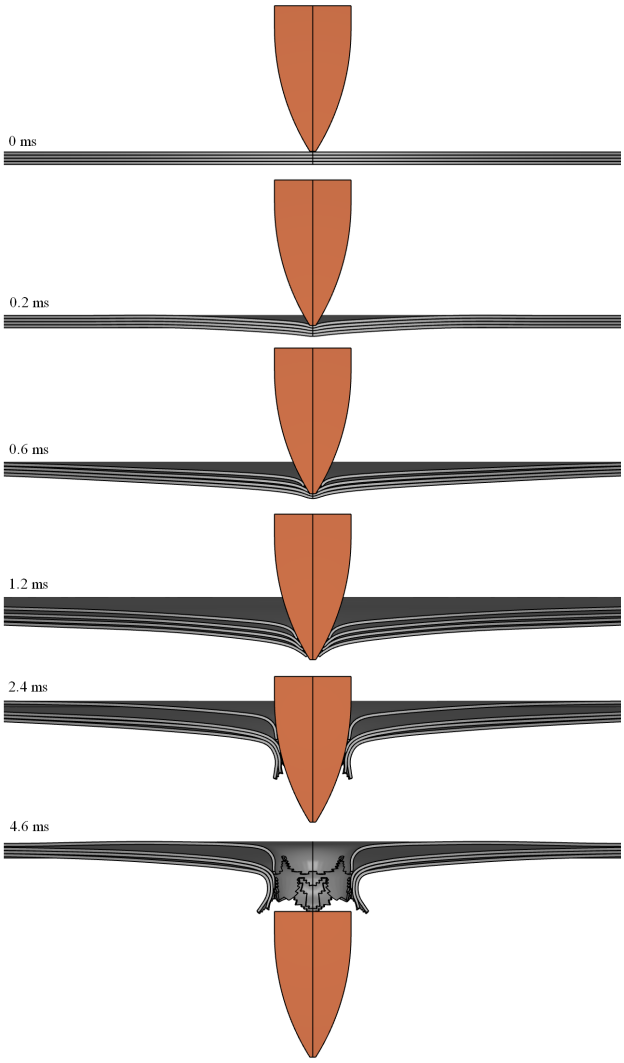


Figure 19: Image series displaying the predicted perforation process of 4 plates by the ogival-ended impactor ($v_i$ = 14.0 m/s, $v_r$ = 11.6 m/s).

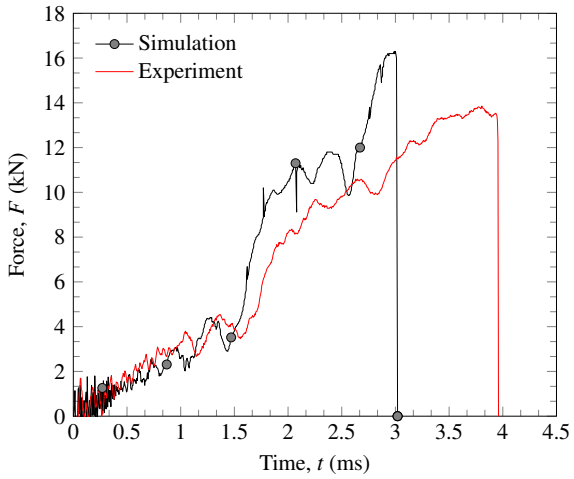


(a) Blunt-ended impactor

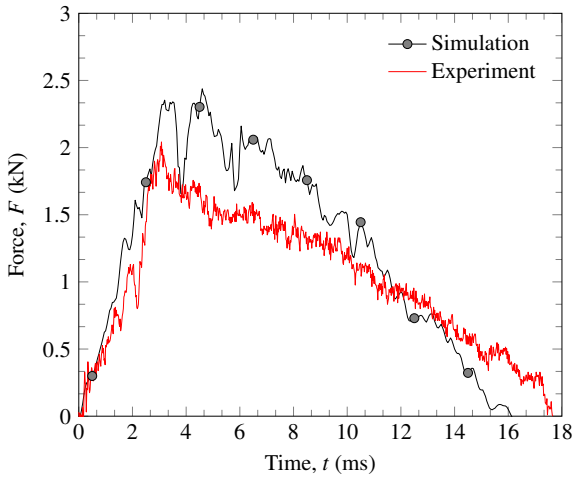


(b) Ogival-ended impactor

Figure 20: Comparison of numerical and experimental results for (a) the blunt-ended impactor ($v_i$ = 5.9 m/s, $v_r$ = 3.0 m/s) and (b) the ogival-ended impactor ($v_i$ = 3.6 m/s, $v_r$ = 1.9 m/s).